Supplementary Information

In-situ-grown silver–polymer framework with coordination complexes for functional artificial tissues

Songlin Zhang[1], Yibing Deng[2], Alberto Libanori[3], Yihao Zhou[3], Jiachen Yang[1], Trinny Tat[3], Lin Yang[1], Wanxin Sun[4], Peng Zheng[2], You-Liang Zhu[5*], Jun Chen[3*], Swee Ching Tan[1*]

[1]Department of Materials Science and Engineering, National University of Singapore, 9 Engineering Drive 1, Singapore, 117574, Singapore

[2]State Key Laboratory of Coordination Chemistry, Chemistry and Biomedicine Innovation Center (ChemBiC), School of Chemistry and Chemical Engineering, Nanjing University, Nanjing, Jiangsu, 210023, P.R. China

[3]Department of Bioengineering, University of California, Los Angeles, Los Angeles, CA 90095, USA

[4]Bruker Nano Surface and Metrology, 30 Biopolis Street #09-01, The Matrix, Singapore 138671

[5]State Key Laboratory of Supramolecular Structure and Materials, College of Chemistry, Jilin University, Changchun 130012, China

[*]To whom correspondence should be addressed: Y.-L.Z. (youliangzhu@jlu.edu.cn), S.W.T (msetansc@nus.edu.sg), J.C. (jun.chen@ucla.edu)

This PDF file includes:

Other Supplementary Materials for this manuscript include the following:

Supplementary Methods

Rheological measurements. Rheological properties were characterized using a rheometer (Anton Paar, MCR 302) with a parallel plate of Ø 50 mm (for solutions) and Ø 25 mm (for gels). All tests were run at ~23 °C. The shear rate was set in the range of 0.1 to 1000 1/s for the viscosity test. The angular-frequency sweep spectra were obtained by controlling the shear strain at 1 % over the frequency range of 0.1–200 rad/s. The oscillation-strain-sweep spectra in the range of 0.1–2000% were recorded by setting a constant angular frequency of 0.628 rad/s. The step-strain measurement was conducted by alternating the oscillatory strain between 1% and 1000%, respectively (angular frequency was fixed at 0.628 rad/s).

Uniaxial tensile tests. For all tests, sample dimensions were cut into ~20 mm in gauge length, ~4 mm in width. Thickness was estimated at ~200 μm from the SEM image. Sandpaper tabs were attached to both ends of the samples to ensure good grasp strength during tests. Tensile tests were run on a universal tensile testing machine at a speed of 20 $mm \cdot min^{-1}$. For consecutive stretching-releasing, an interval rest time (0, 1, 5, 10, and 20 min) was adjusted to allow strain recovery. All cyclic tests were performed on the same sample. Strain hysteresis phenomenon was observed for PANSion.

UV-Vis spectroscopy. The UV-Vis spectra were recorded from 800 to 250 nm using model Agilent Cary 5000 for PAN and PANSion solutions and DMF solvent. The solutions were diluted by ten times from the original PAN or PANSion solutions before the test. A quartz cuvette was used for the UV-Vis spectra collection with a path length of 1 cm.

Differential scanning calorimetry (DSC) and thermogravimetric analysis (TGA). DSC results for PANSion films of varying ϕ were obtained using TA instruments DSC 25 model in the temperature range from −50 to 25 °C at a ramping rate of 5 $°C \cdot min^{-1}$ under nitrogen environment. Glass transition temperature (T_g) was derived from the cooling down process. T_g of PAN powder and PAN film was determined by running DSC from 50 to 350 °C at a rate of 5 $°C \cdot min^{-1}$. TGA was utilized to determine the weight percentage of DMF within the as-prepared film samples (TA Instruments Q50). The testing temperature range was from 50 to 600 °C at a ramp rate of 10 $°C \cdot min^{-1}$. The DMF weight percentage was calculated based on the weight change in the temperature range between the onset and endpoint of the second derivative weight change peak (a peak centered at ~175 °C, which was close to the boiling point of DMF, 153 °C). In this study, evaporation instead of decomposition happened to DMF during the temperature ramping.

Scanning electron microscopy (SEM) and energy-dispersive X-ray spectroscopy (EDX). Morphologies of PAN and PANSion were investigated using a field-emission scanning microscope (FE-SEM, Zeiss Supra 300) with an accelerating voltage at 3 kV. Both area mapping and line scanning of EDX were recorded using Oxford Ultim Max silicon drift detector (SDD) at 10 kV, two times higher than the absorption energy of silver at L-edge.

Transmission electron microscopy (TEM). TEM images and corresponding TEM mode EDX spectra were recorded using JEOL JEM 2010F. PANSion film was supported on a copper grid, which was prepared using a similar procedure for C-AFM samples. Briefly, 50 μL of PAN or PANSion (ϕ = 2.0) solution was dropped on a copper grid. Followed that was oven drying at 55

°C for 48 hours. As this procedure was the same as the one used for macroscale PANSion film preparation, the micro-/nanoscale structures of PANSion films observed under TEM should be identical to the structures of macroscale PANSion films. The size of AgNPs was estimated by surveying different TEM images statistically.

Supplementary Texts

Text 1 | Binding energy calculation and CG-MD simulation

1. Binding energy calculation

The binding energies between metal ions and PAN were calculated as the energy difference between the metal-ion-PAN complex (*AB*) and separated metal ion (*A*) and PAN (*B*) by the following equation.

$$E_{binding} = E_{AB} - E_A - E_B \qquad (1)$$

The optimization of configurations and the calculation of energies were all carried out using the Dmol3 module in the Materials Studio 7.0 (Accelrys inc., San Diego). The density functional theory (DFT) method was employed using the gradient corrected (GGA) correlation functional of Perdew and Wang (PW91) with the double numerical plus (DNP) polarization basis set, where the convergence threshold parameters for the optimization are set as 2.7×10^{-4} eV (energy), 0.05 eV/Å (gradient), and 0.005 Å (displacement). With the aid of the DFT calculations, we obtained the binding energy for several different metal ions (see **Supplementary Table 2**).

2. Simulation of radial tensile test

CG-MD simulations are employed in uniaxial tension tests. The beads are integrated forward in time according to Newton's equations of motion with a time step Δt = 0.005 τ_0 (τ_0 = 1.63 ps). We construct a pure PAN simulation system of 200 chains with a chain length of 500 beads and a composite system (PANSion), including PAN of 200 chains with a chain length of 500 beads, 10 Ag nanoparticles, and 33,333 $AgNO_3$ molecules. The equilibrium structures of the pure PAN and PANSion are obtained by annealing from 0.7 (380 K) to 0.55 (300 K) for 3×10^7 time steps in NPT ensemble (about ~0.24 μs). The structure of PANSion was amorphous according to the calculated crystallinity (3%). The periodic boundary conditions in *X* and *Y* directions are removed, while the periodic condition in the *Z* direction was kept. The Weeks–Chandler–Andersen (WCA) potential was employed as a boundary condition in *X* and *Y* directions in annealing simulations and removed in uniaxial tension tests to make the interface of the samples with air.

The tension test simulations of PAN (T = 0.1 for the semicrystalline structure) and PANSion (T = 0.55 for the amorphous structure) are performed for one stretching process and two stretching-releasing cycles respectively. The simulation per stretching-releasing cycle runs 3.2×10^7 time steps (about ~0.26 μs). The uniaxial tension simulations are performed by a constant tension rate of 3.12×10^{-7} strain unit per MD step with the maximum strain = 5. The stress was calculated by the

pressure multiplied by the initial cross-sectional area of samples. The Herman's orientation factor ($f_{(H)}$) was calculated by

$$f_{(H)} = \frac{3\langle\cos^2\theta\rangle - 1}{2}, \quad (2)$$

where θ is the angle between the bonds of PAN chains and the stretching direction. The ratio of regenerated bonds (RRB) is calculated by

$$RRB(t) = 1 - \langle\frac{N_t}{N_0}\rangle, \quad (3)$$

where N_0 is the number of neighboring PAN beads of a Ag^+ bead where they form coordination complexes, and N_t is the number of the initially recognized and recorded neighboring PAN beads of the Ag^+ bead that remain acting as its neighbors at the time of *t*. The CG simulations are all performed on GPU chips[1].

Text 2 | Single-molecule force spectroscopy (SMFS)

After forming $[Ag(-C\equiv N)_x]^+$ coordination complexes, it was not feasible to assess the molecular interactions *in-situ* within the free-standing PANSion film due to the dense and entangled chain network. A common way reported in the literature is to conduct SMFS measurements by dispersing the target molecule in a buffer solution where the molecule chain can move freely[2, 3]. This also applies to our material. However, it is worth pointing out that DMF is a good solvent for preparing PAN solutions because of interactions between the formamide group (from DMF) and nitrile group (from PAN). Therefore, the polymer chain of PAN can move freely in DMF solvent, as verified by SMFS results (**Extended Data Fig. 3b**). On top of this, if there are any additional interactions between PAN polymer chains, such as $[Ag(-C\equiv N)_x]^+$ complexes, SMFS results should show corresponding characteristics. Additionally, DMF is a suitable solvent for the SMFS test as it possesses a low saturated vapor pressure of ~306 Pa (at 20 ℃) that is even lower than that of water (2333 Pa 20 °C), thus avoiding the issue of fast solvent evaporations. Nevertheless, note that the testing solutions for SMFS still need to be confined in a small chamber with a cover to avoid any phase change since DMF and H_2O (from the air) are miscible with each other. Especially when a drop of PAN or PANSion solution was exposed in air, liquid-to-solid phase separation could be observed (**Extended Data Fig. 3a**).

AFM-SMFS results shown in **Extended Data Fig. 3b**–**e** provide direct evidence on the formation of $[Ag(-C\equiv N)_x]^+$ complexes among PAN chains. Although dry PAN film is strong in mechanical strength because of abundant nitrile-nitrile interactions, no characteristic force rupture peaks were observed from AFM-SMFS tests due to the aforementioned free movement of PAN molecular in DMF solvent. The strong inter- or intramolecular strength from nitrile-nitrile interactions was broken because of the good dissolvability of DMF. On the contrary, several characteristic force rupture peaks were recorded for the PANSion solution. These results confirm that the addition of Ag^+ leads to the formation of $[Ag(-C\equiv N)_x]^+$ metal-ligand complexes that enhance the inter- or intramolecular interactions of PAN molecules. Therefore, the effective-molecular-length (EML) of the PANSion chain was expected to be longer than that of PAN due to the cross-linking effect of $[Ag(-C\equiv N)_x]^+$ complex. Further cyclic SMFS test shows that PANSion network (cross-linked by $[Ag(-C\equiv N)_x]^+$ complex) was extensible (*i.e.*, stretchable). We also speculate that the dissociation-reformation of $[Ag(-C\equiv N)_x]^+$ is a dynamic process based on the obtained high stretchability of PANSion film and the calculated binding energy. Ideally, if the

force rupture peak during the first stretching-releasing cycle reappears during the next stretching-releasing cycle, then the dynamic nature of $[Ag(-C\equiv N)_x]^+$ can be experimentally validated via SMFS test. However, we did not obtain such results (with only force rupture peak) despite many trials. The possible reason is that the theoretical length of the PAN chain in our study was relatively short (~ 380 nm for an average molecular weight of 150,000) compared to other elastic polymers such as polydimethylsiloxane (PDMS). Therefore, for most SMFS tests, we only observed one force rupture peak; thus, no dissociation-reformation dynamic process was recorded (**Extended Data Fig. 3f**). Nevertheless, modifications to either the starting material of PAN (higher molecular weight) or the AFM-SMFS setup in the future study may provide further evidence for our conjecture with potential new outcomes.

Text 3 | PANSion solutions and free-standing PANSion film

PANSion solutions with varying ϕ were prepared using 2 wt% PAN solution as the base (**Supplementary Table 3**). Accordingly, the mole ratio λ, referring to the mole of –C≡N groups on PAN chains divided by the mole of Ag^+ from the ionization of $AgNO_3$, was calculated using the following equation:

$$\lambda = \frac{\frac{m_{(PAN)}}{M_{w(PAN)}} \times \frac{M_{w(PAN)}}{M_{w([C_3H_3N])}}}{\frac{m_{(AgNO_3)}}{M_{w(AgNO_3)}} \times 1} \qquad (4)$$

where $m_{(PAN)}$ and $m_{(AgNO3)}$ can be found in **Supplementary Table 3.** $M_{w(PAN)}$, $M_{w(AgNO3)}$, and $M_{w([C3H3N])}$ were 150,000 g/mol, 169.87 g/mol, and 53.06 g/mol, respectively. Note that the repeat unit of $[C_3H_3N]$ was used to estimate the mole of –C≡N groups on each PAN molecule chain.

Since the formation of $[Ag(-C\equiv N)_x]^+$ complex is a gradual process, rheological properties of PANSion solutions after storing for a varying time, were characterized to assess the molecular chain network structure, which is critical for the free-standing film's mechanical properties. The viscosity-shear rate results indicated a more entangled network at a higher ϕ due to the increased cross-linking density from $[Ag(-C\equiv N)_x]^+$ complexes. Additionally, the gelation of ϕ = 2.0 takes a shorter time than other solutions, which also confirms a high cross-linking density is formed at a higher ϕ. When the formed network entanglement within PANSion is not sufficiently strong, it can be disrupted by shear force, displaying a water-like behavior when the shear rate is greater than 10 s^{-1}. Once gelation occurs, gel of ϕ = 2.0 exhibits a shear-thinning behavior.

Compared to the SMFS characterization of assessing the mechanical property of PANSion chain at molecular level, the amplitude- and frequency-sweep rheological tests of PANSion solutions describe mechanical properties of the entangled chain network at macroscale (but in a wet state instead of dry state) that is closer to the actual network structure of the dry PANSion film. Especially for PANSion gels, they possess a densely cross-linked network that resembles (with a high probability) the structure of the thermally dried PANSion film. Thus, the viscoelastic behavior of PANSion gels in a broad strain range is also applicable for the PANSion film that is highly stretchable. Compared to PANSion solutions, the disappearance of the lower Newtonian flow region of PANSion gels in the viscosity-shear rate curves indicates the formation of a three-dimensional physical network structure [4]. The fast response of PANSion gels while alternating between 1% and 1000% strain can be utilized to explain the strain recovery performance of PANSion film.

For free-standing PANSion film preparation, the temperature is an important factor, as pointed out in our previous study [5]. The concentration of $[Ag(-C\equiv N)_x]^+$ is also critical to achieving high stretchability as implied by the gel transition of PANSion solutions at varying ϕ (~10 days for ϕ = 2.0, ~30 days for ϕ =1.0). Therefore, thermal heating was applied as a more efficient way to accelerate the formation of a cross-linked network comparing to the gel transition at room temperature. More importantly, an exceeding amount of DMF solvent can be removed, which usually limits the mechanical properties of gels (too much solvent) prepared at room temperature. Note that a too low or too high temperature may lead to the failure of preparing free-standing PANSion film. If a drying temperature is too low (i.e., <35 ℃), on the one hand, it may require a longer preparation time due to the low evaporation rate of DMF solvent. On the other hand, the excessive amount of DMF solvent cannot be removed once the entanglement of the molecular chain network is formed at this drying temperature because most of the solvent molecules are trapped within the network, requiring an even higher temperature to evaporate. However, if the starting drying temperature is too high (*i.e.*, >90 ℃), the solvent evaporation can induce a phase separation between the cross-linked molecular chain network and the remaining solvent, resulting in a porous and less stretchable structure.

Text 4 | *In-situ*-grown AgNPs

The redox activity of DMF has already been reported previously [6, 7]. Studies have shown that DMF can act as a reducing agent under appropriate conditions, even at room temperature. Our study also observed the reduction effect of DMF both at room temperature and elevated temperature. By following Liz-Marzán's work [8], the reduction process involved in the reaction at room temperature can be described as:

$$HCONMe_2 + 2Ag^+ + H_2O \rightarrow 2Ag(0) + Me_2NCOOH + 2H^+$$

$$Me_2NCOOH \rightarrow CO_2 + Me_2NH$$

The successful reduction can be verified by the increased electrical conductivity of as-prepared PANSion film. Several things are worth pointing out here. First, the reduction rate from Ag(I) to Ag(0) by DMF is slow at room temperature, which can be implied from the increased intensity of the characteristic absorption peak of UV-Vis spectra of PANSion solution at 422 nm after days-long storage. Second, the size of AgNPs can be tuned by adjusting the starting concentration of $AgNO_3$ and reaction temperature. For instance, Liz-Marzán and co-workers reported AgNPs' size distributions of 6.5–11 nm for reaction at 20 ℃ and 8–17.4 nm for reaction at 60 ℃. This observation also agrees with our statistical analysis of AgNPs size. Third, the distribution of *in-situ* formed AgNPs within the PANSion film theoretically expresses an ideal distribution of a percolative conductive network without any aggregations, benefiting from the homogeneous phase of starting solutions. Fourth, only a partial amount of Ag(I) is reduced to Ag(0) during the thermal drying of the PANSion solution because of the limited, reducing capability and evaporation of DMF. Overall, together with $[Ag(-C\equiv N)_x]^+$ metal-ligand complex and *in-situ* formed AgNPs, the as-prepared PANSion film is highly stretchable and electrically conductive.

Indirectly, the increased electrical conductivity of PANSion film also verifies the successful reduction of Ag(I) by DMF. The conductivity can be explained by a percolation theory that analyzes the conductivity of conductor-insulator composites as a function of conductor volume fraction, ψ. The overall conductivity is written as:[9, 10]

$$\sigma = \sigma_0 \left(\frac{\psi - \psi_c}{1 - \psi_c}\right)^n \qquad (5)$$

where σ_0 is the conductivity of a AgNP network, ψ_c is the minimum volume fraction where the network remains electrically connected (often termed the percolation threshold), and n is the percolation exponent. But one should note that the exact amount of AgNPs (either in weight or volume percentage) in the as-prepared PANSion film is not explicitly calculated in this study. On the one hand, it is not accessible to determine the percentage of reduction from Ag(I) to Ag(0). From the TEM images of PANSion film, AgNPs are well distributed. Thus, we can potentially calculate the volume percentage of these nanoparticles by reconstructing the 3D tomography of several representative sites (this will be our future study).

Additionally, electrical conductivity can be obtained by adding AgNPs, silver flakes or other conductive fillers into PAN film (*i.e.*, mixing conductive fillers and PAN solution first and then thermal drying). However, using this approach, the PAN film after drying showed no stretchability due to no formation of $[Ag(-C\equiv N)_x]^+$ metal-ligand complexes. Using this approach, other elastomers such as styrene butadiene rubber (SBR), nitrile butadiene, PDMS, and polyurethane (PU) are more suitable than PAN polymer. However, preparations of these conductive materials may suffer from difficulties of homogeneously dispersing conductive fillers and compromising the polymer matrix's compliance and stretchability.

Text 5 | Piezoresistive sensing applications.

1. PANSion film as a strain sensor

Due to the *in-situ* formed AgNPs, PANSion film itself is responsive to mechanical stimulus as a piezoresistive strain sensor. This feature is unique compared to other coordination complex-based elastic polymers that usually require additional conductive fillers to enable such sensing properties. **Supplementary Fig. 22** shows a PANSion film of ϕ = 2.0 that has a resistance in the range of MΩ. Additionally, the PANSion film of ϕ = 2.0 displays the highest electrical conductivity among the prepared samples, reaching a value of 0.076 $S \cdot m^{-1}$. Although this PANSion film is not as conductive as some conductive polymers (e.g., polypyrrole, polyaniline, or PEDOT:PSS, etc.), we demonstrated that our PANSion film is a good candidate for thin-film-based strain sensor applications because the relationship between resistance change ($\Delta R/R$ in %) versus external strain (%) is much more important than the absolute value of electrical conductivity for piezoresistance applications. **Supplementary Fig. 23b** shows the relationship between $\Delta R/R$ (%) and strain (%). Here the sensitivity (or gauge facture, GF) is defined as the ratio of $\Delta R/R$ (%) over strain (%). Three regions of sensing performance can be recognized. For strain in 0–200% and 200–500%, the sensitivity of 0.614 and 0.64 were obtained, respectively. A higher sensitivity of 1.42 was observed for strain greater than 500%. PANSion film also shows decent stability of maintaining the $\Delta R/R$ (%) value while holding the strain at 200%. Based on the above features, we demonstrated that PANSion film is sensitive for monitoring various activity positions of finger moving, such as flexion angle (or amplitude) and frequency. Just a single PANSion film can successfully capture other limb motions at different activity amplitude and frequency, such as elbow bending and ankle plantarflexion.

To be more accurate in assessing the performance of PANSion film, the resistance change, $\Delta R/R$ (%), at both small and large strains were collected using a linear motor. At small strains,

such as 1% or 2%, the corresponding $\Delta R/R$ (%) is around 0.5% and 1%, respectively. Although the absolution value is small, the electrical response signal is recognizable and can be distinguished from noises. At large strain, such as 200–400%, PANSion film displays good repeatability of sensing response. One thing worth pointing out here is the up-shifting of the sensing data baseline. Although the up-shifting brings troubles for data processing, especially for real-time application, the relative intensity of resistance changes during the cyclic test at 200–400% is stable, indicating that by incorporating a customized data processing algorithm, a stable sensing performance can be delivered. This speculation can be supported by the sensing data from the 500-cycle test at 10% and 50% strain (**Supplementary Fig. 28**). Although the baseline up-shift occurred during the cyclic test, the relative intensity of resistance change at both 10% and 50% in a short period is almost the same. Nevertheless, this baseline up-shift issue still requires more studies to figure out the fundamental causes.

2. PANSion solution enabled sensing textile

By increasing the concentration of PAN, the viscosity of as-prepared PANSion solutions can also be increased accordingly. When the solution is sufficiently viscous, it can be applied as dip-coating ink for fabrics surface treatment. **Supplementary Fig. 29-30** display the spreadability (i.e., penetration property) of PAN and PANSion solutions (ϕ = 2.0) with varying concentrations of PAN from 2 wt% to 12 wt%. On the one hand, higher concentration results in a decreased spreadability for both solutions due to the increased viscosity. On the other hand, to guarantee the formation of a continuous and conductive PANSion network after drying the coating solutions, a high concentration of PAN is required. In this study, 10 wt% of PAN solution was used for PANSion solution (ϕ = 2.0) preparation to balance the trade-off between penetration effectiveness and successful conductive network formation.

3. PANSion fiber spinning

From the 10 wt% PANSion solutions (ϕ = 2.0), a PANSion fiber can be successfully drawn once the optimal network entanglement density is achieved after storing the PANSion solution for a few days. **Extended Data Fig. 6a** shows the spinnability of PANSion solutions (ϕ = 2.0) with 2 wt% to 12 wt% of PAN. It is apparent that 10 wt% and 12 wt% of PANSion solutions demonstrate a good spinnable feature. Interestingly, the PANSion fiber can be directly drawn from a PANSion solution in the air (**Extended Data Fig. 6b**).

Text 6 | Surface-capacitive system for touch sensing

Since PANSion film is electrically conductive, a surface-capacitive system can be adapted to develop a touch-sensitive film using PANSion by applying a small voltage to the PANSion film that is collected with two electrodes as schemed in **Supplementary Fig. 33a**. When a finger touches the PANSion film surface, two things happen simultaneously, as explained by the following descriptions. On the one hand, a finger touch, as a capacitive load, can result in a closed circuit where the touch point is grounded. Therefore, the equivalent capacitance of the whole system is increased due to the apparent capacitance from finger touch. On the other hand, once the touch point is grounded, a potential difference is caused between the electrodes and the touch point, concomitantly leading to a current flow from the electrode through the finger. Moreover, the current magnitude is proportional to the distance between the touch point and the electrode.

Here, the coefficient α and 1–α is used to describe the position of a touch point. Consequently, the capacitance of $\boldsymbol{C}_{\mathrm{EDL},\alpha}$ and $\boldsymbol{C}_{\mathrm{EDL},1-\alpha}$ varies as the touch point moves along the PANSion film. **Supplementary Fig. 33b** shows the circuit diagram where a finger touch is applied.

Note that different conductors possess a unique capacitance load that can result in different changes of the whole system's equivalent capacitance. Thus, by carefully designing the pre-recognition threshold of capacitance change values for each tested object, the PANSion film can be employed as a "skin" with a human-like "feeling" to tell what object is conducting the touch task. To enable such function, we programmed an algorithm to differentiate touch objects based on the sensing response feature. First, the data is collected as follows:

1. Start collecting the data at the moment when the object is touching the material.
2. Keep touching the material for a period of t seconds.
3. Stop collecting data at the moment when the object is detached.
4. Compute the average of the collected data over time t.

Repeat steps 1 – 4 twenty times for three different objects (i.e., finger, glove, and metal), resulting in 60 samples in total. Given the above data, we trained a machine learning algorithm to classify the object which touches the material. The Decision Tree with entropy criterion is selected to perform the classification task. We performed cross-validation as follows:

1. Randomly split the collected data (40 samples) into training data (60%) and test data (40%)
2. Use the training data to train the decision tree
3. Apply the trained decision tree to perform classification on the test data
4. Compare the prediction to the true label and calculate the accuracy.

Repeat steps 1 – 4 ten times and compute the averaged accuracy. Our experimental results demonstrate that we can obtain 100% accuracy via the decision tree.

Text 7 | PANSion film based actuator with self-sensing capability

1. Self-sensing actuation

Compared to other reported hydrogel-based ionic conductors, one advantage of PANSion film is its free-standing feature that expresses sufficiently high strength for actuation application. While for most actuation materials reported in the literature, post-treatments, including surface coating of a conductive network, are required to obtain electrical monitoring signal of actuation status while performing a task. Particularly, our PANSion film can simultaneously execute the actuation task and output an electrical signal corresponding to its specific actuation status. First, the amplitude of actuation (*i.e.*, displacement, Δd) can be controlled by adjusting the applied pressure. Both small and large amplitudes can be recognized from corresponding electrical signals. More importantly, the electrical signal changes from low to high intensity are real-time, together with the corresponding actuation patterns. Second, the actuation frequency is also recognizable from the electrical signals. While performing actuation of weight-lifting, the starting point of lifting and releasing is indicated by the sudden increase or decrease of resistance change ($\Delta R/R$). A holding status of actuation is detected by a stable value of ($\Delta R/R$). Furthermore, different releasing procedures can be differentiated as the change rate of $\Delta R/R$ is different. As a proof-of-concept, we also demonstrated the object manipulation ability using a self-sensing gripper (both proprioception and exteroception) based on a two-chamber configuration of PANSion actuators

(**Extended Data Fig. 8**). While transferring objects at different temperatures, the corresponding electrical signals are different, which can be utilized to distinguish whether the object is cold or warm or at room temperature.

2. Areal strain calculation

The strain in terms of area expansion (%) during actuation is roughly estimated by assuming the contour of the deformed PANSion film is half of an ideal spheroid (as indicated by the dash-line in **Extended Data Fig. 7a**). The coefficient *a* and *b* are equal to each other, while *c* is the maximum deformation height of PANSion film (i.e., Δ*d*) that depends on the applied external pressure. As a special case of a tri-axial ellipsoid, the surface area of a spheroid (a = b) can be expressed as follow:

when $c < a$:

$$S_{\text{oblate}} = 2\pi a^2 \left(1 + \frac{c^2}{ea^2} \cdot arctanh(e)\right) \qquad \text{where } e^2 = 1 - \frac{c^2}{a^2}$$

or
when $c > a$:

$$S_{\text{prolate}} = 2\pi a^2 \left(1 + \frac{c^2}{ae} \cdot arcsin(e)\right) \quad \text{where } e^2 = 1 - \frac{a^2}{c^2}$$

Since *c* is a variant that depends on the applied pressure, in this study, we applied the following equation for approximation to calculate the surface area regardless of the value of *c* (i.e., for both $c < a$, $c > a$ and $c = a$):

$$S \approx 4\pi \sqrt[p]{\frac{(ab)^p + (ac)^p + (bc)^p}{3}} \qquad (6)$$

where p =1.6 for spherical ellipsoids (*i.e.*, spheroid for our case). Thus, the area strain of PANSion film in terms of area expansion during actuation can be calculated as follows for a specific *c* (i.e., Δ*d*):

$$\varepsilon_{area} = \frac{\frac{S}{2} - \pi a^2}{\pi a^2} \qquad (7)$$

Extended Data Fig. 7b presents the comparison between displacement (mm) and areal strain (%) when applied pressure varies. A linear relationship between displacement and area strain can be speculated for both directions of inward and outward deformation of PANSion film-based actuator.

3. Performance matrix evaluation

Performance can be further improved by designing an even stronger PANSion membrane or applying other actuation mechanisms. For comparison and transparency purposes, we calculated the actuation performance matrix to deliver a comprehensive investigation of our PANSion membrane-based actuator.

During actuation, although the maximum displacement of weight-lifting depends on the applied pressure, the time of one actuation cycle when lifting a load of 50 g is nearly instantaneous, ~0.5–0.8 s (**Supplementary Video 4**). The average specific work (W_{average}) is calculated as:

$$W_{\text{average}} = \frac{(m_{\text{load}} \cdot g) \cdot \Delta d_{\text{average}}}{m_{\text{membrane}}} \quad (8)$$

where m_{load} and m_{membrane} are the weight of lifting load (50 g) and PANSion membrane (30.4 mg), respectively. $\Delta d_{\text{average}}$ is the average maximum displacement during five weight-lifting cycles (21 mm). g is the gravitational acceleration. Thus, the average specific work is calculated to $W_{\text{average}} \approx$ 365 J/kg. Considering the short actuation time, $t_{\text{actuation}}$ (~0.5 – 0.8 s), the average specific power (P_{average}) can be calculated as:

$$P_{average} = \frac{W_{average}}{t_{actuation}} \quad (9)$$

Thus, P_{average} is ~456 – 730 W/kg.

To assess the energy utilization of the PANSion actuator, thermodynamic efficiency, η, is calculated as:

$$\eta = \frac{E_{output}}{E_{intput}} \quad (10)$$

where E_{output} and E_{intput} are the energy output (actuation induced weight-lifting) and energy input (pressure-induced PANSion membrane deformation), respectively which can be calculated as:

$$E_{output} = (m_{load} \cdot g) \cdot \Delta d \quad (11)$$

and

$$E_{intput} = \int_0^{V_0} P(V) dV \quad (12)$$

where V is the deformation volume of the PANSion membrane induced by pressure. The volume can be roughly estimated as half of a spheroid that can be calculated as:

$$V = \frac{1}{2} \times \frac{4}{3} \pi abc \quad (13)$$

By plugging in parameters, the calculated thermodynamic efficiency of η is ~40.2%.

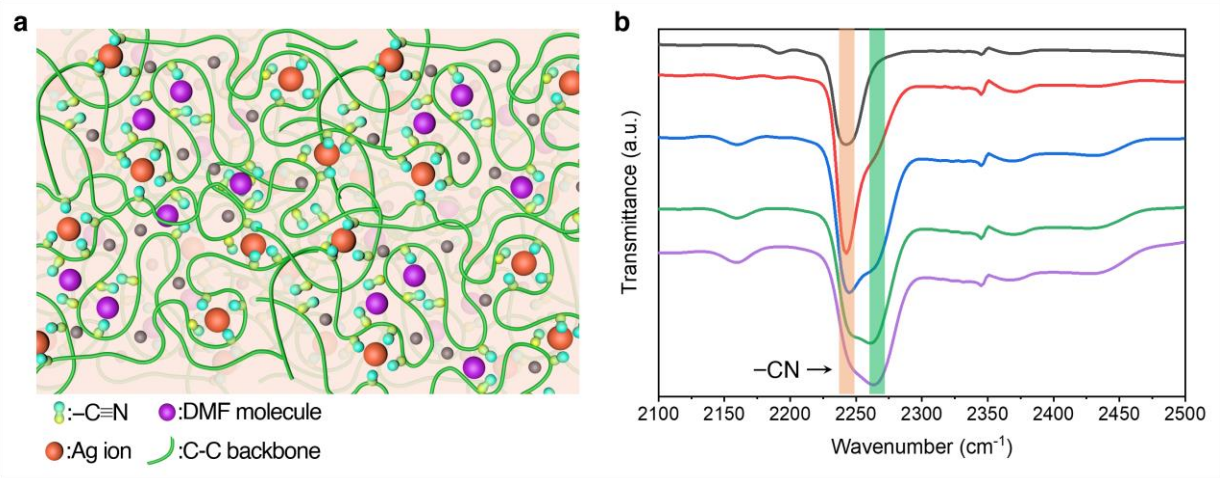

Supplementary Figure 1 | Molecule structures of PANSion polymer. a, Schematic of PANSion network with various interactions. **b**, The corresponding FTIR spectrum of PAN (black line) and PANSion films (colored lines). Additional shoulder peak (shaded area in green) next to –CN (shaded area in orange) was assigned to the formation of $[Ag(-C\equiv N)_x]^+$ complexes.

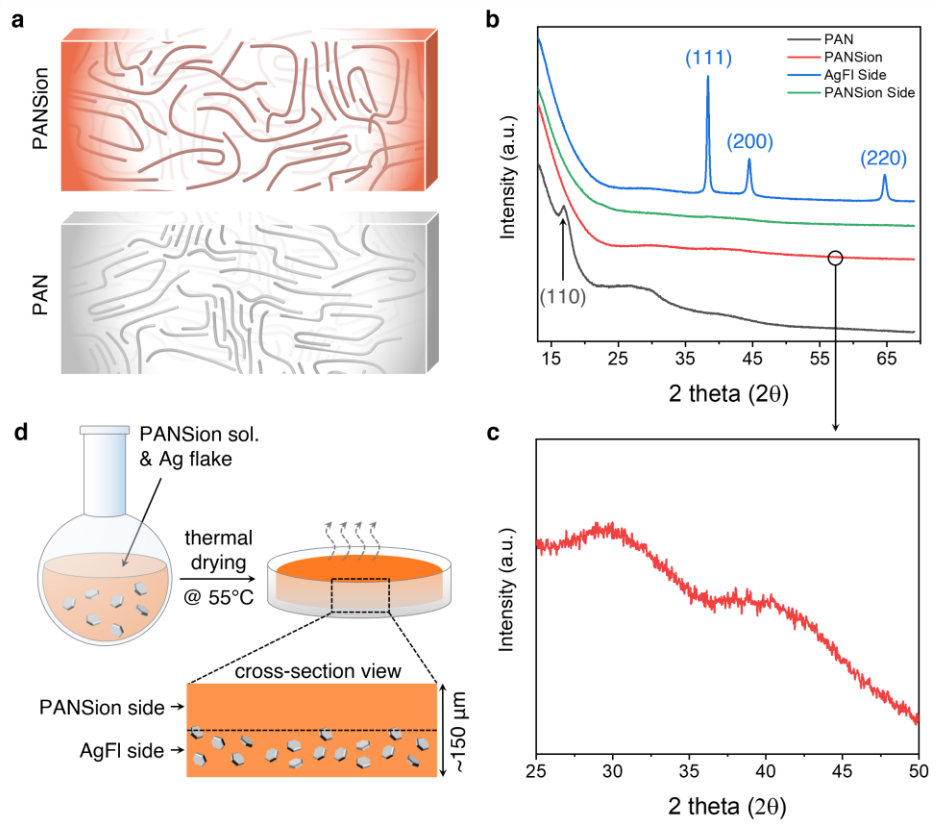

Supplementary Figure 2 | Microstructures of PAN and PANSion films. a, Schematic of amorphous PANSion and semicrystalline PAN films. **b** and **c**, Power X-ray diffractions. **d**, Schematic process of preparing PAN/silver flake composite (PAN/AgFl), which shows a Janus structure of two different sides: PANSion side and AgFl side.

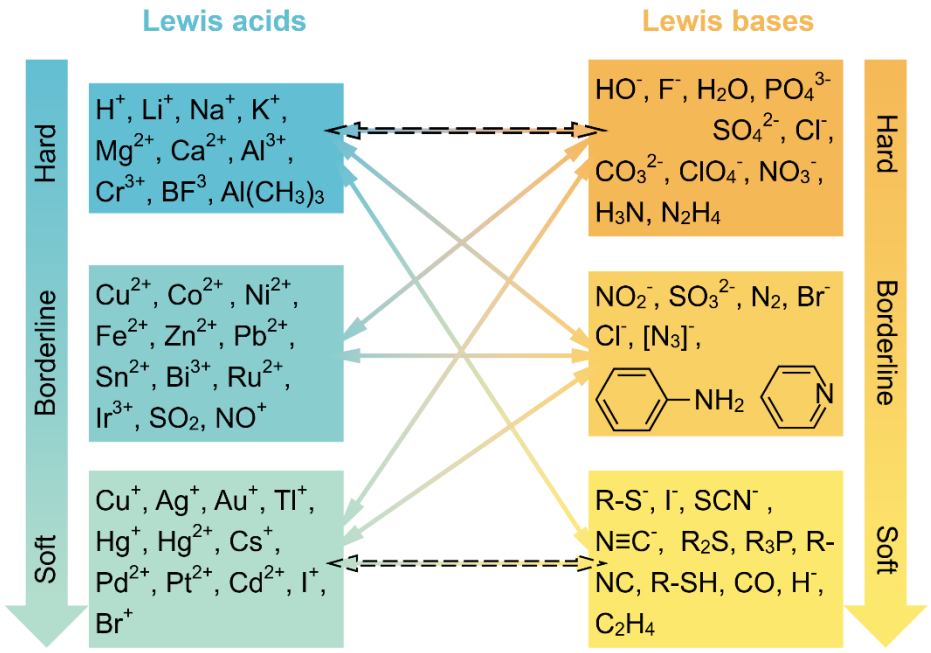

Supplementary Figure 3 | Lewis acid and base theory. Arrows-connectors indicate the possible coordination complexes between metal ions and ligands.

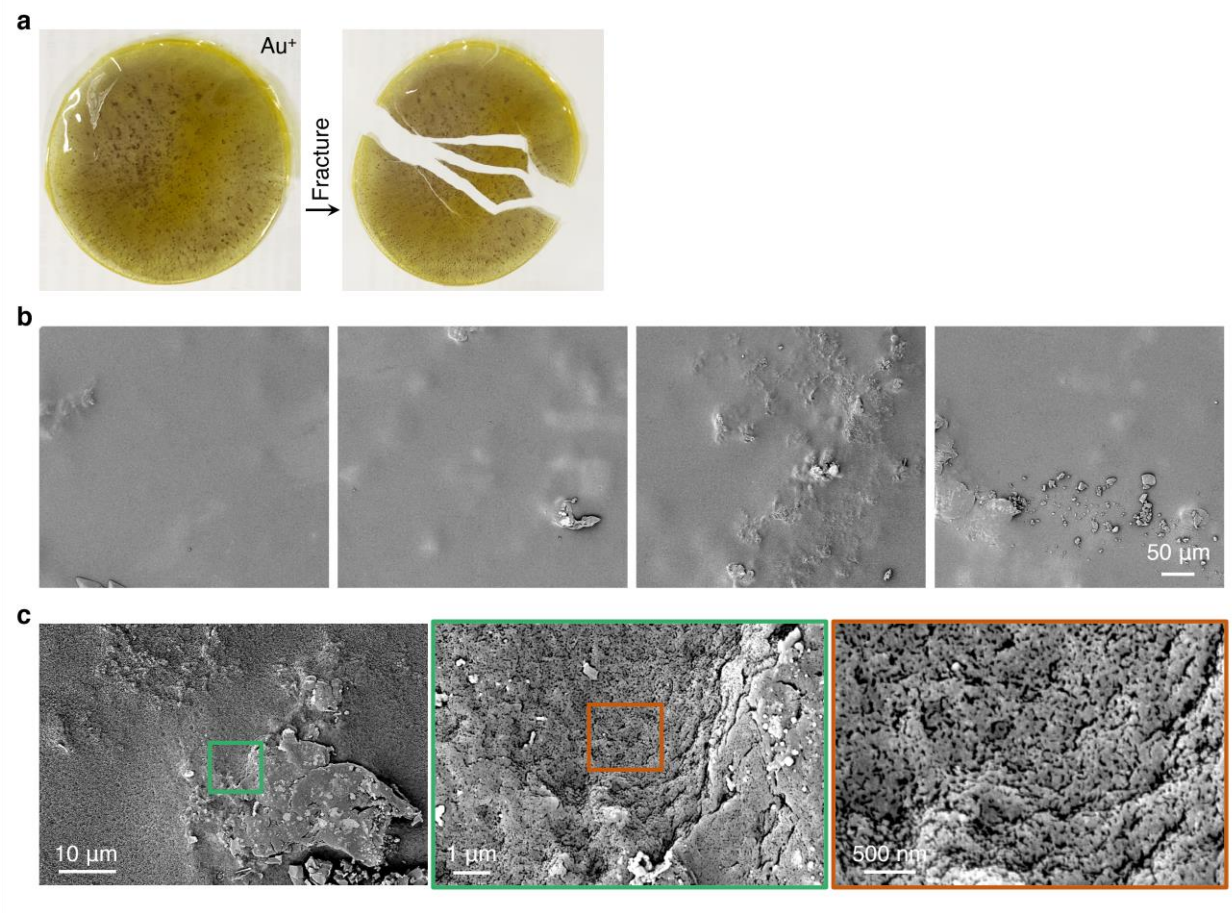

Supplementary Figure 4 | Composite film of PAN with gold chloride. a, As-prepared film and its fracture. No stretchability was observed during stretching. **b**, SEM images at low magnification showing clusters. **c**, SEM images at high magnification showing the detailed morphology. Both macro-/micro-scale morphologies of PAN–Au^{+} composite film are different from PANSion film, although the binding energy of Au^{+} and Ag^{+} to –CN is similar, implying in-depth investigation is still needed in the future.

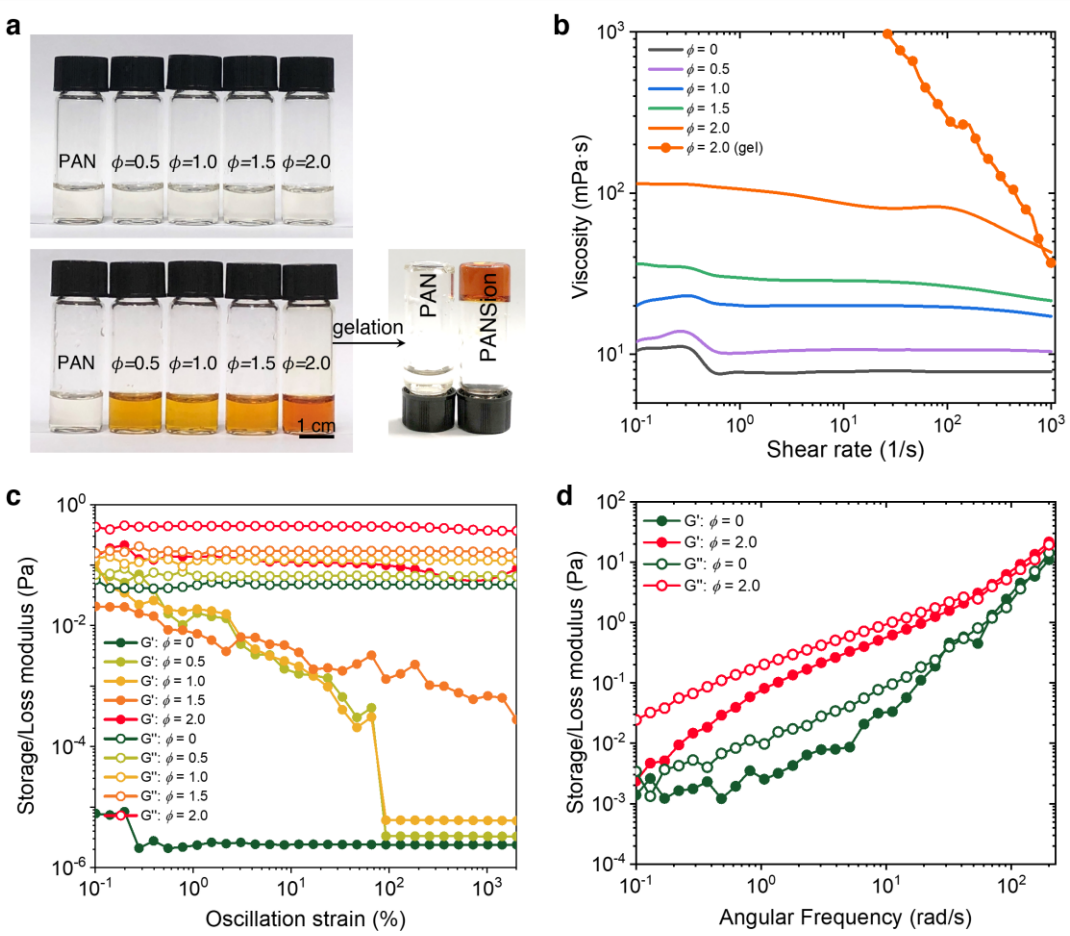

Supplementary Figure 5 | Viscosity of PANSion solutions with varying ϕ. a, Images showing the as-prepared PANSion solutions and solutions after storing for several days. Gelation occurs for ϕ = 2.0 at the earliest compared to other solutions. **b** and **c**, The viscosity of PANSion solutions as a function of shear rate (b) and their strain-sweep properties (c). **d**, Comparison of frequency-sweep results between PAN and PANSion (ϕ = 2.0) solutions.

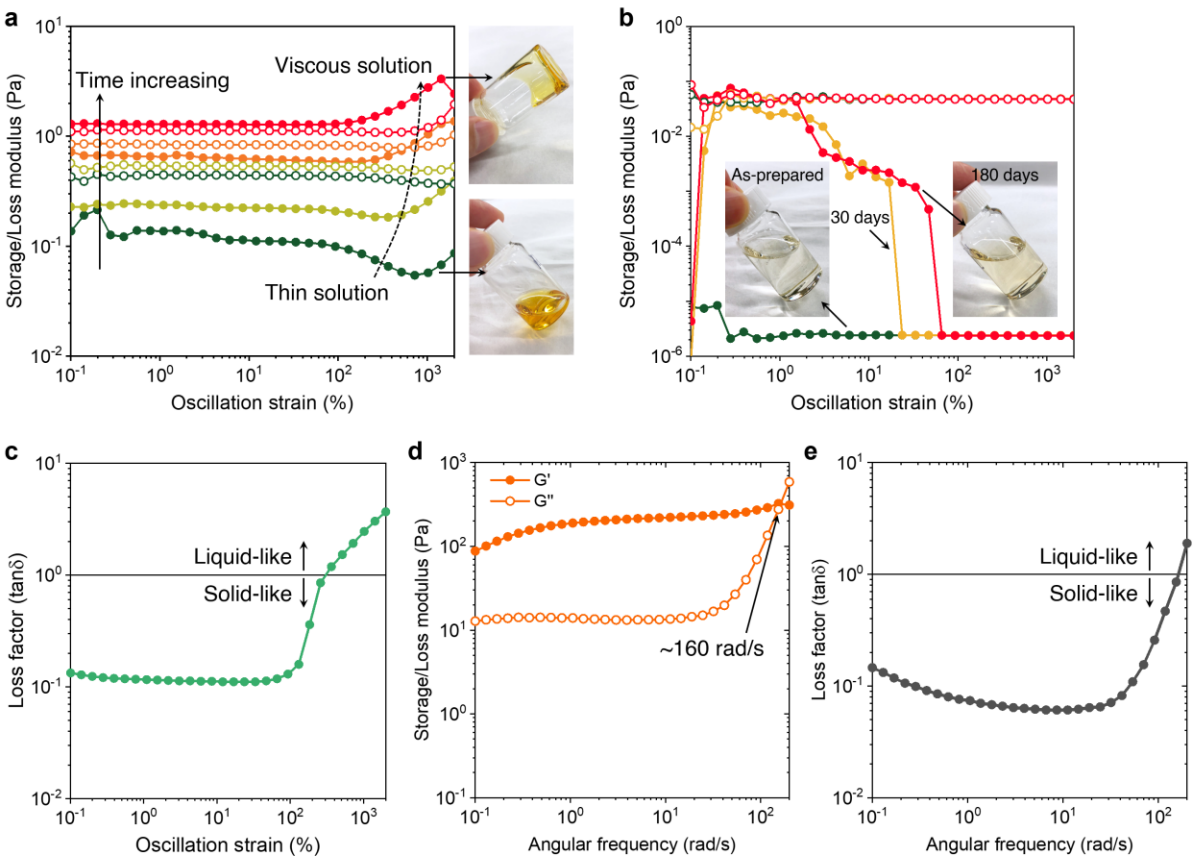

Supplementary Figure 6 | Rheological properties of PANSion solutions and gels. a, The corresponding modulus change when a thin PANSion solution transforms to a viscous one, then to a gel. **b**, Monitoring modulus of PAN solution after storing for various time. **c**, Strain-sweep-derived loss factor for PANSion gel (ϕ = 2.0). **d** and **e**, Frequency sweep (D) and corresponding loss factor (E) for PANSion gel (ϕ = 2.0).

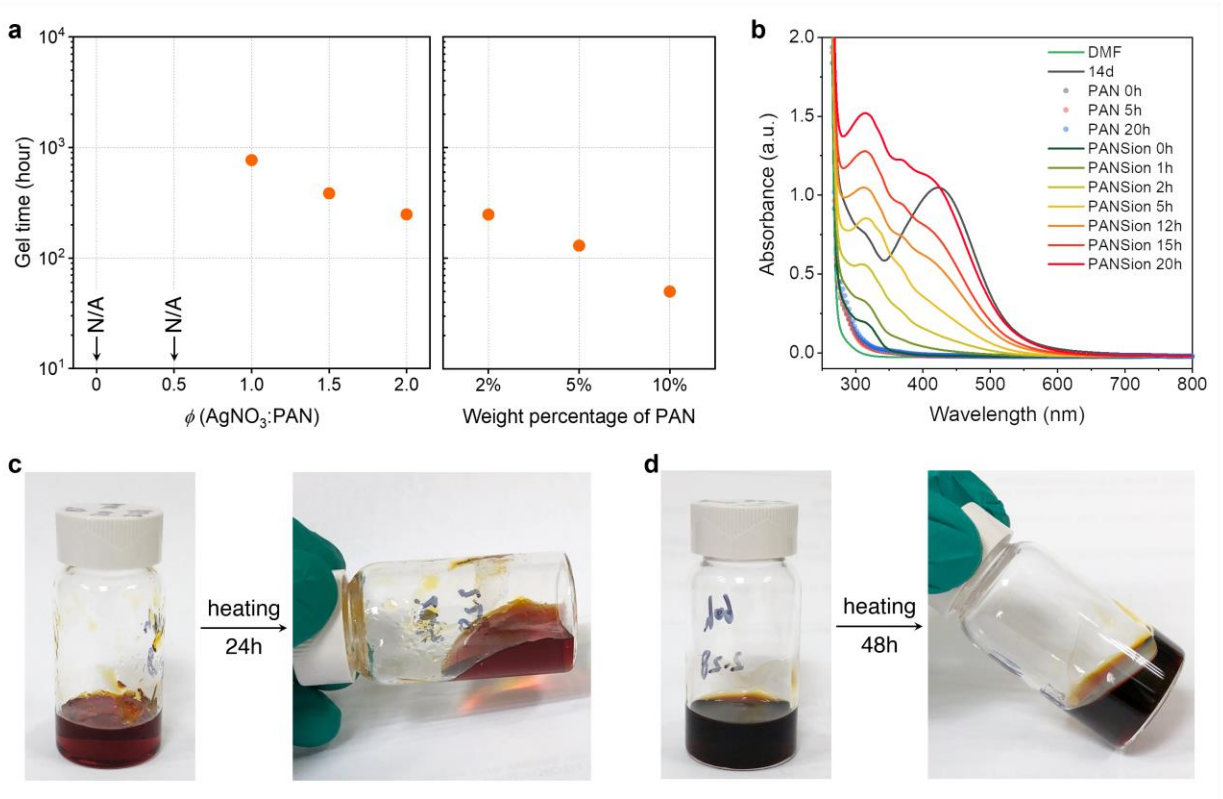

Supplementary Figure 7 | Gelation of PANSion solutions. a, Gel time as a function ϕ and concentration of PAN. **b**, UV-Vis spectra of PANSion solutions after heating for varying times. **c** and **d**, Gelation occurs for ϕ = 2.0 after heating for 24 hours (c), and the gel becomes even stronger after 48 hours of heating (d).

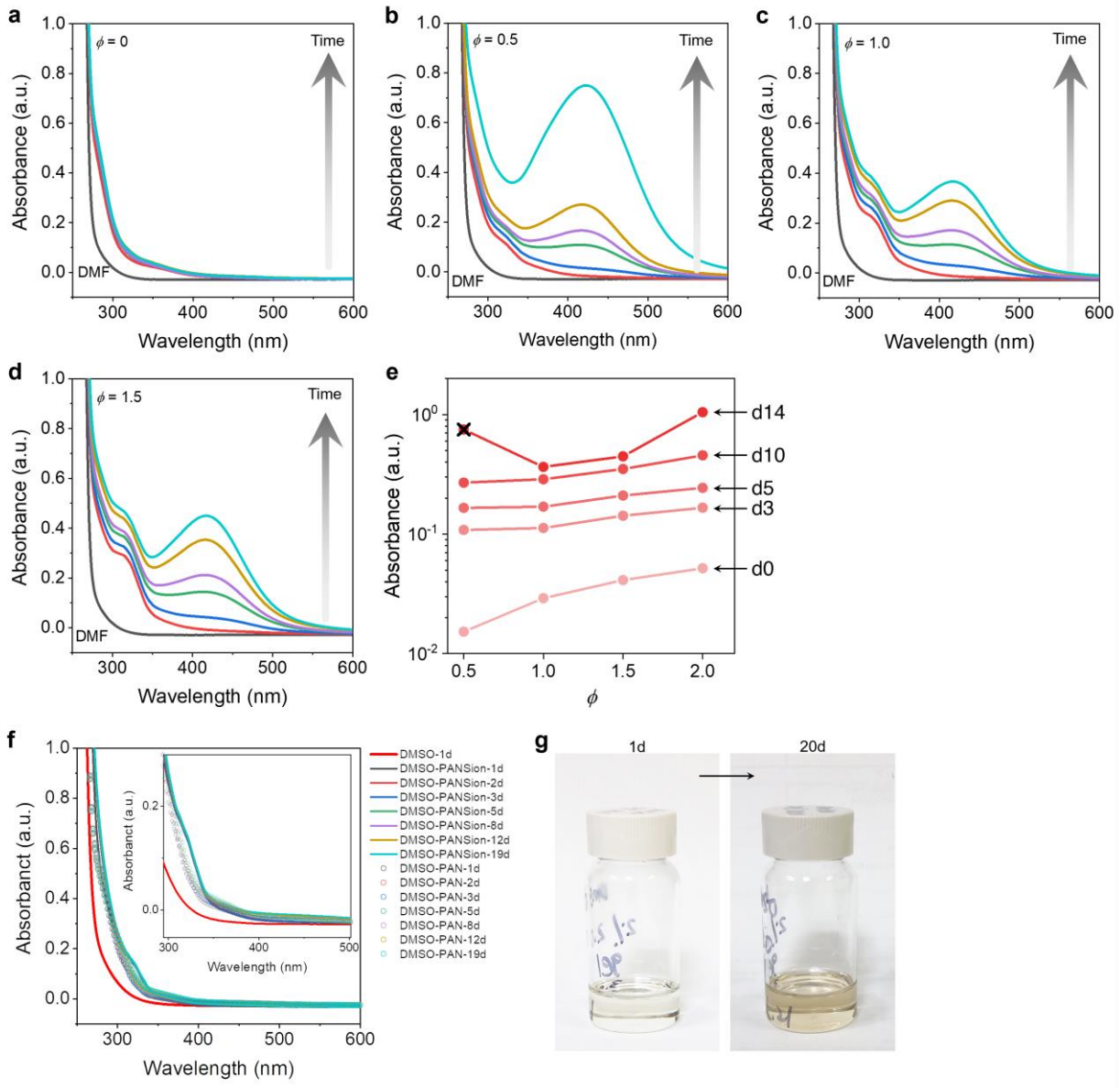

Supplementary Figure 8 | UV-Vis spectra of PAN and PANSion solutions after various storage times. a, PAN solution with no obvious change during the observation period. **b**–**d**, PANSion solutions with increased intensity at 422 nm (from the localized surface plasmon resonance effect of AgNPs), indicating the successful reduction of silver ions by DMF. **e**, The higher intensity at a higher ϕ is ascribed to the more reduced AgNPs. **f** and **g**, UV-Vis spectra of DMSO-PANSion solutions with no characteristics at 422 nm (f) and no obvious color change due to the existence of AgNPs in solutions (g).

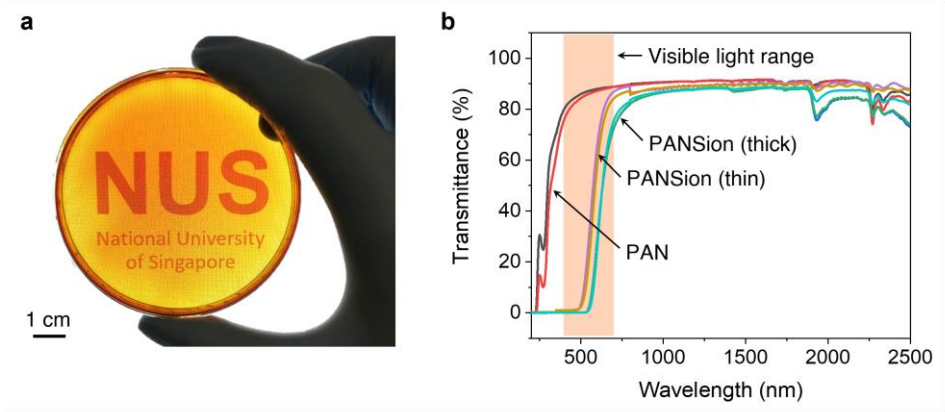

Supplementary Figure 9 | PANSion film and its transparency. a, PANSion film in a petri dish. **b**, The transmittance of PAN and PANSion films in Vis-NIR range.

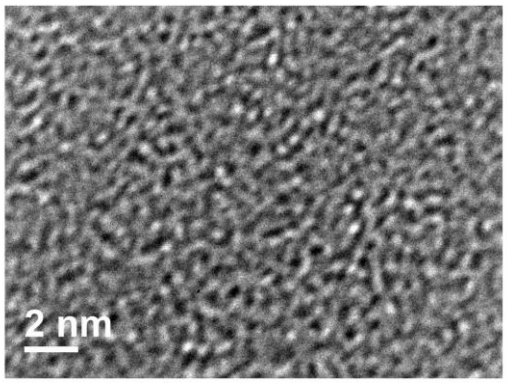

Supplementary Figure 10 | TEM image of PAN film.

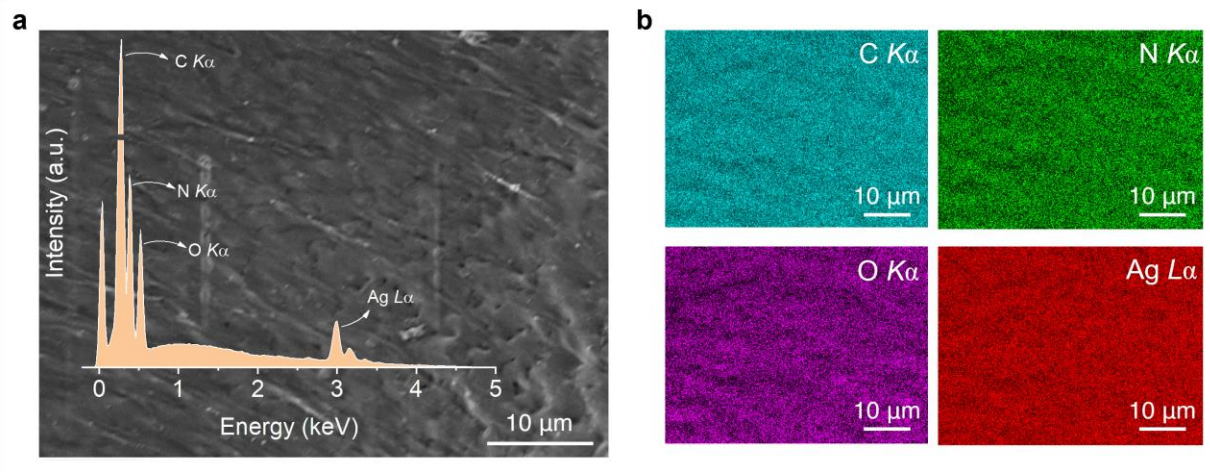

Supplementary Figure 11 | SEM image and EDX mapping results of PANSion film. a, A representative SEM image of PANSion film. Inset is the corresponding EDX spectrum. **b**, Elemental mappings from EDX results for PANSion film including carbon (C), nitrogen (N), oxygen (O), and silver (Ag) elements.

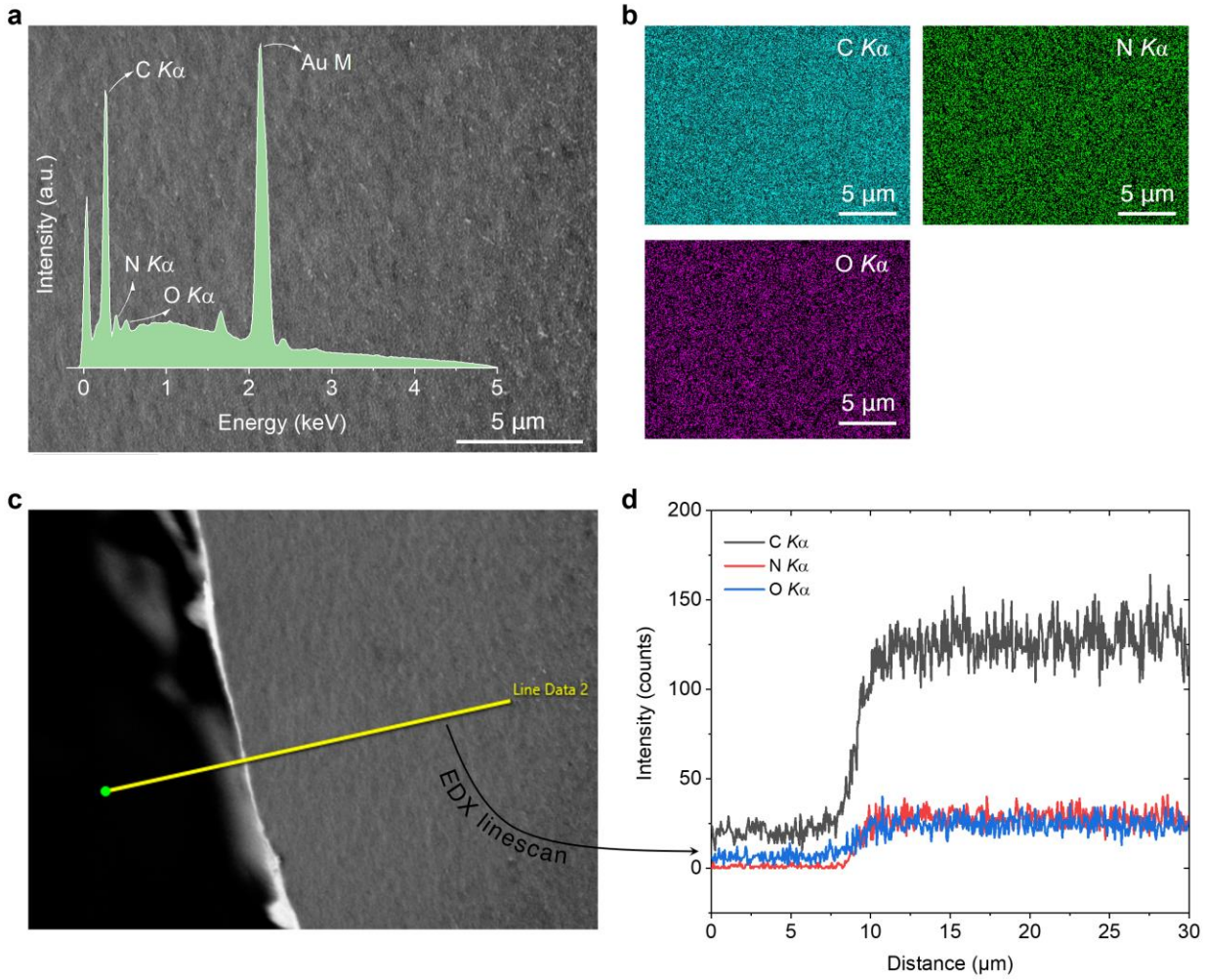

Supplementary Figure 12 | SEM images and EDX mapping results for PAN film. a, A representative SEM image of PAN film. Inset is the corresponding EDX spectrum. **b**, Elemental mapping from EDX results for PAN film including carbon (C), nitrogen (N), and oxygen (O) elements. **c**, A cross-sectional SEM image with a line marker where the linescan profile of EDX data was collected. **d**, Element distribution along a through-thickness direction (from the line marker area in (c)) for PAN film.

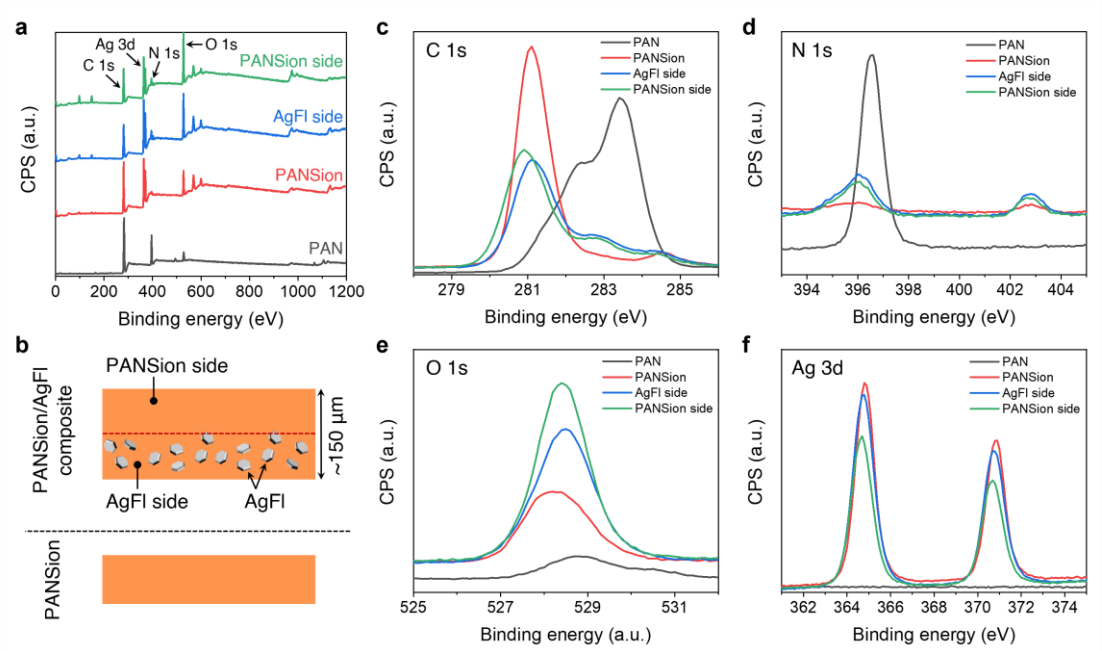

Supplementary Figure 13 | XPS results for PAN and PANSion. a, Survey X-ray photoelectron spectroscopy (XPS) spectra of PAN, PANSion, and PANSion/AgFl composite. **b**, Schematics showing the structural difference between PANSion and PANSion/AgFl composite. **c**–**f**, High-resolution XPS spectra for C 1s (c), N 1s (d), O 1s (e), Ag 3d (f).

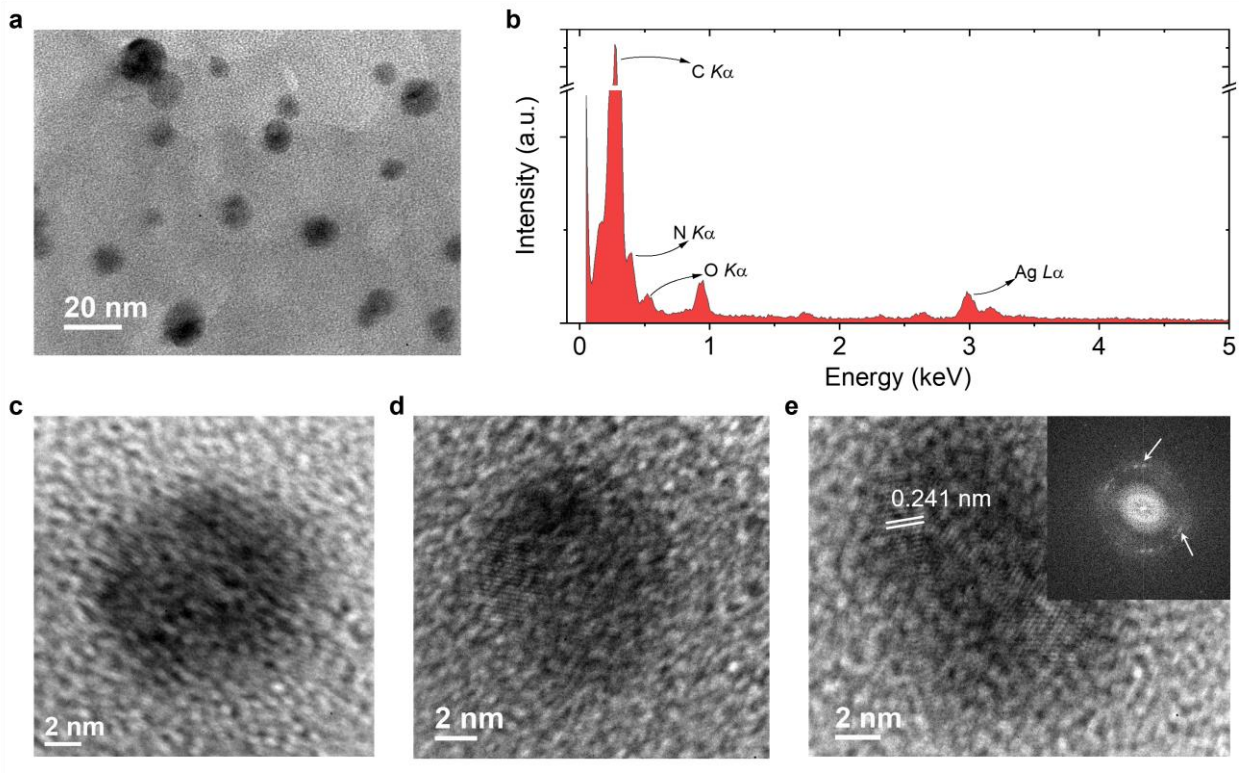

Supplementary Figure 14 | TEM images of PANSion film and the corresponding TEM mode EDX spectrum under. a and **b**, TEM image of PANSion film with AgNPs well embedded and distributed within the polymer matrix (a) and the corresponding TEM mode EDX spectrum (b). **c** and **d**, TEM images of AgNPs at high magnification from different locations. Since the AgNPs are wrapped with a PANSion polymer matrix, the crystalline structure is not explicitly observed. **e**, The lattice structure of a AgNP and the corresponding FFT (inset).

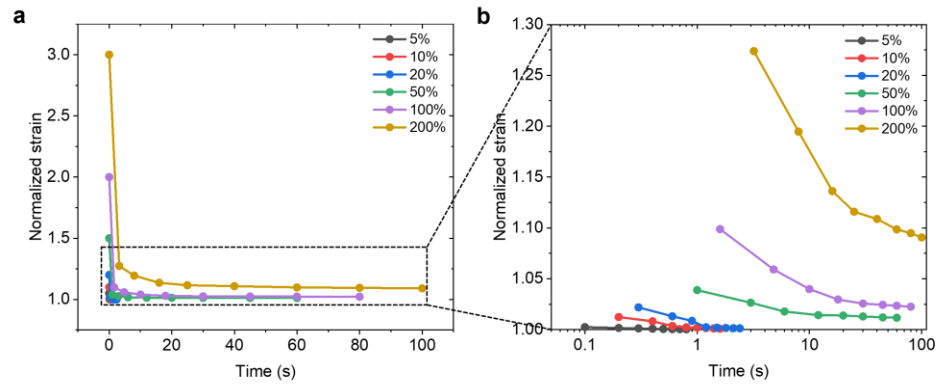

Supplementary Figure 15 | Strain recovery of PANSion film as a function of time. a, The normalized strain after releasing from a specific strain (5% to 200%) as a function of time. **b**, Replot of data in (a) at log scale of time (x-axis) without the initial data point for each strain. It is clear that once the applied strain was released, the PANSion film immediately (within a few seconds) recovered to 105% of its original length for most cases (strain < 100%). For a larger strain (> 200%), a longer time is needed for the recovery, and a residual strain was observed.

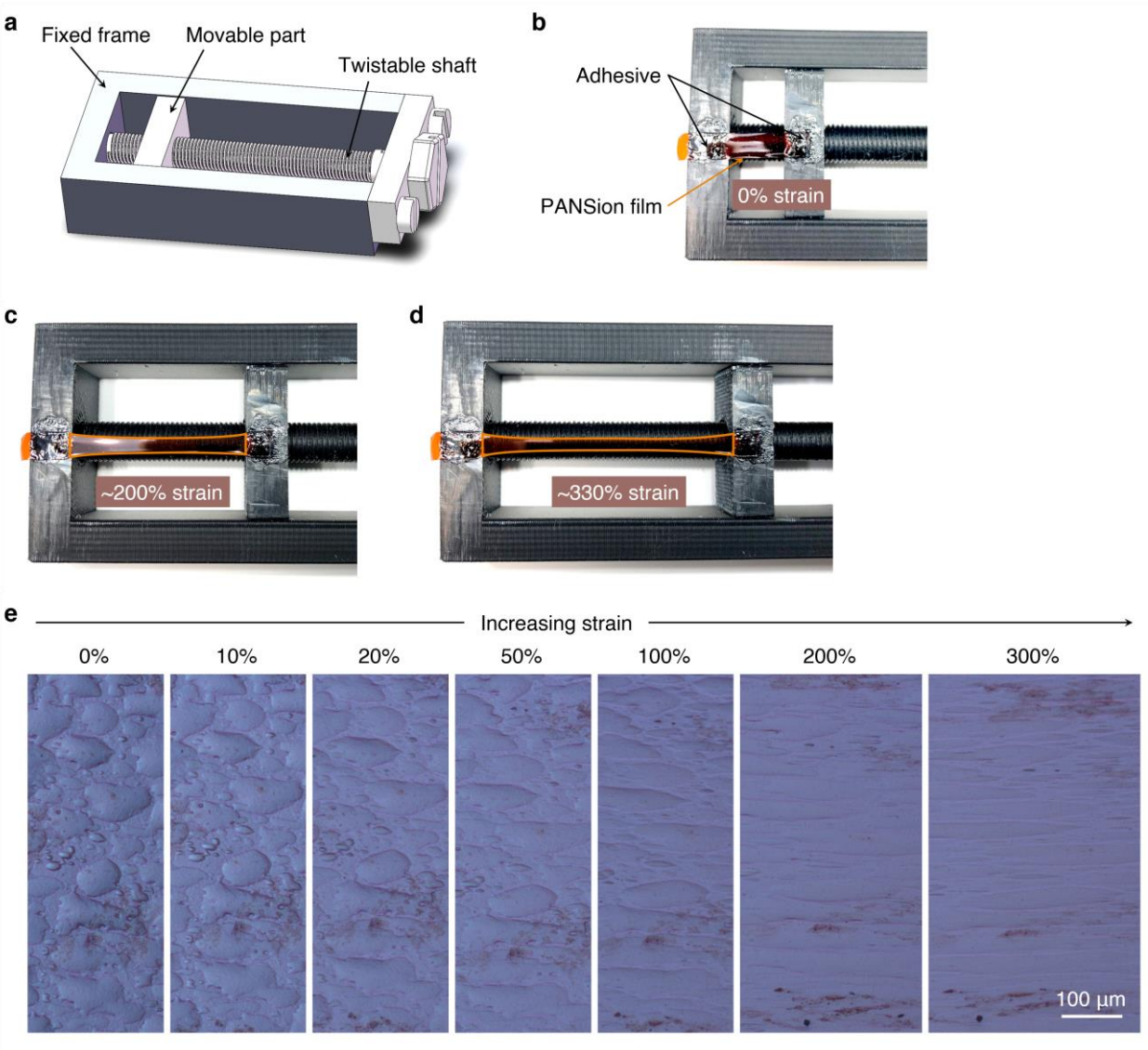

Supplementary Figure 16 | *In-situ* observation on the stretching of PANSion film under an optical microscope. a, The design of a tool used to stretch PANSion film for *in-situ* observation. **b**–**d**, Pictures showing a PANSion film after being stretched to different strains. **e**, Optical images showing the surface morphology change of PANSion film while undergoing a continuous stretching from 0% to 300%. No cracks were observed during stretching.

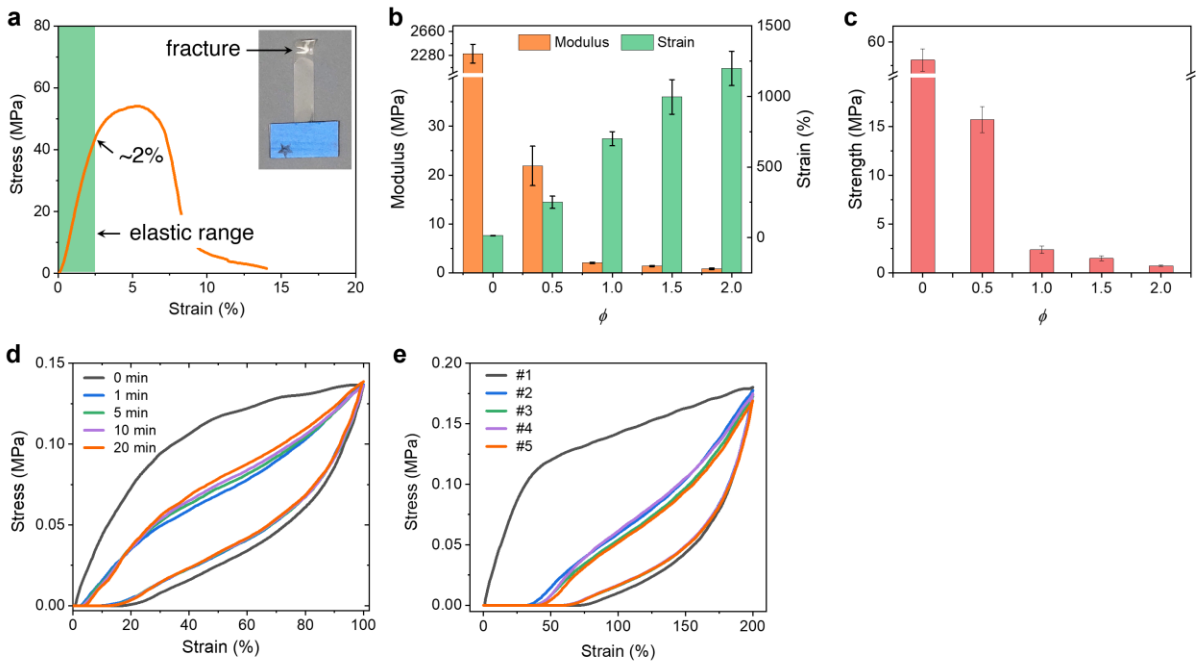

Supplementary Figure 17 | Mechanical properties of PAN and PANSion films. a, Stress-strain curve of PAN film with an elastic strain of ~2%. **b** and **c**, Derived modulus and failure strain (b) and strength (c) of PANSion films with various ϕ. **d** and **e**, Cyclic stretching-releasing of PANSion film (ϕ = 2.0) with different rest times (d) and continuous stretching (e).

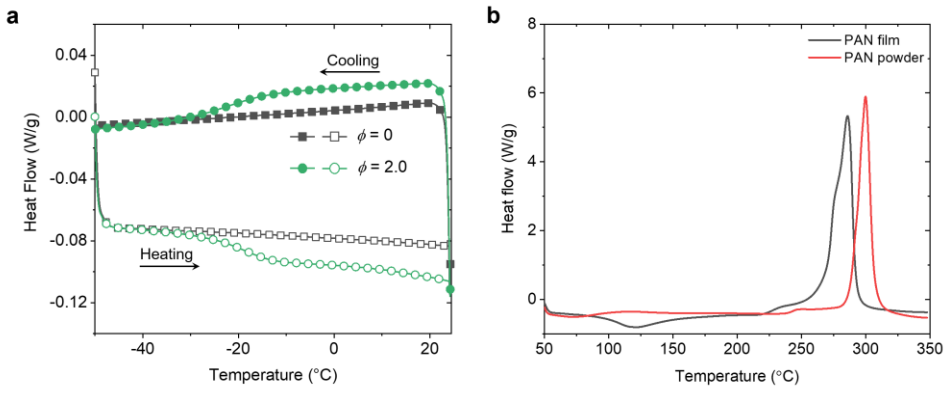

Supplementary Figure 18 | DSC results of PAN and PANSion films. a, Heat flow as a function of temperature, including the cooling stage from 25 ℃ to –50 ℃ and heating stage from –50 ℃ to 25 ℃. Glass transition temperature around –28 ℃ was observed for PANSion film while no recognizable phase transition temperature was found for PAN film in this temperature range. **b**, Heat flow curves of PAN film and original PAN powder (as received from the supplier) from 50 to 350 ℃.

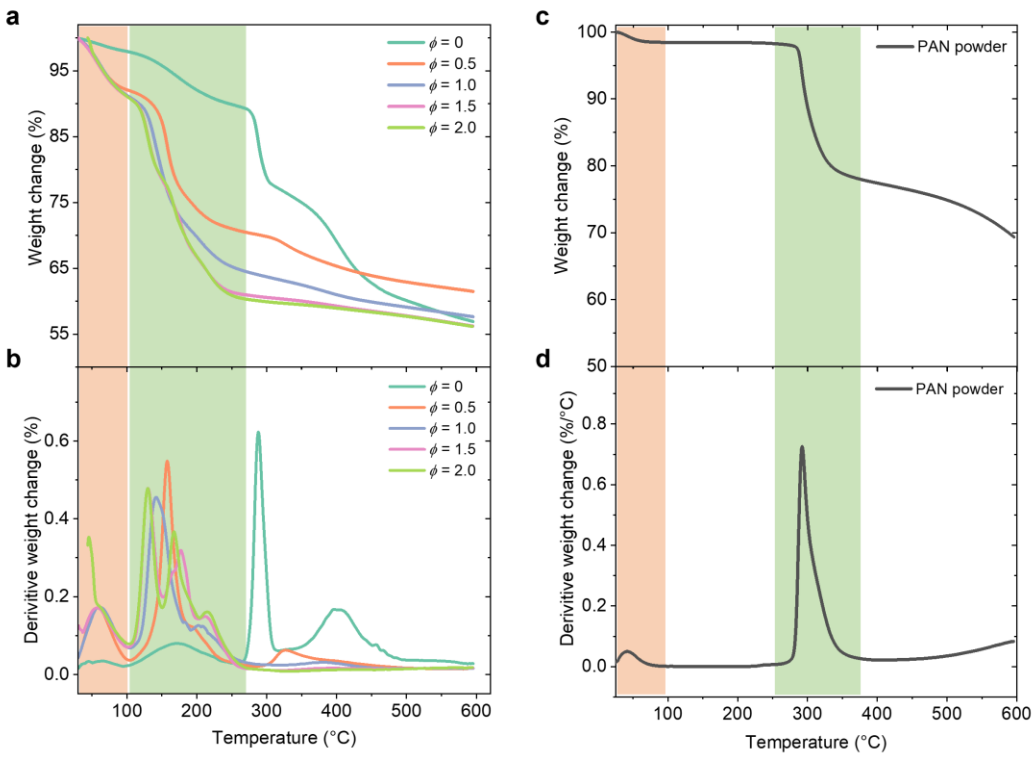

Supplementary Figure 19 | TGA results of PAN and PANSion films. a and **b**, Weight changes (a) and derivative weight changes (b) as a function of temperature from 30 ℃ to 600 ℃ for PAN and PANSion films. **c** and **d**, Weight change (c) and derivative weight change (d) as a function of temperature from 30 ℃ to 600 ℃ for original PAN powder (as received from the supplier).

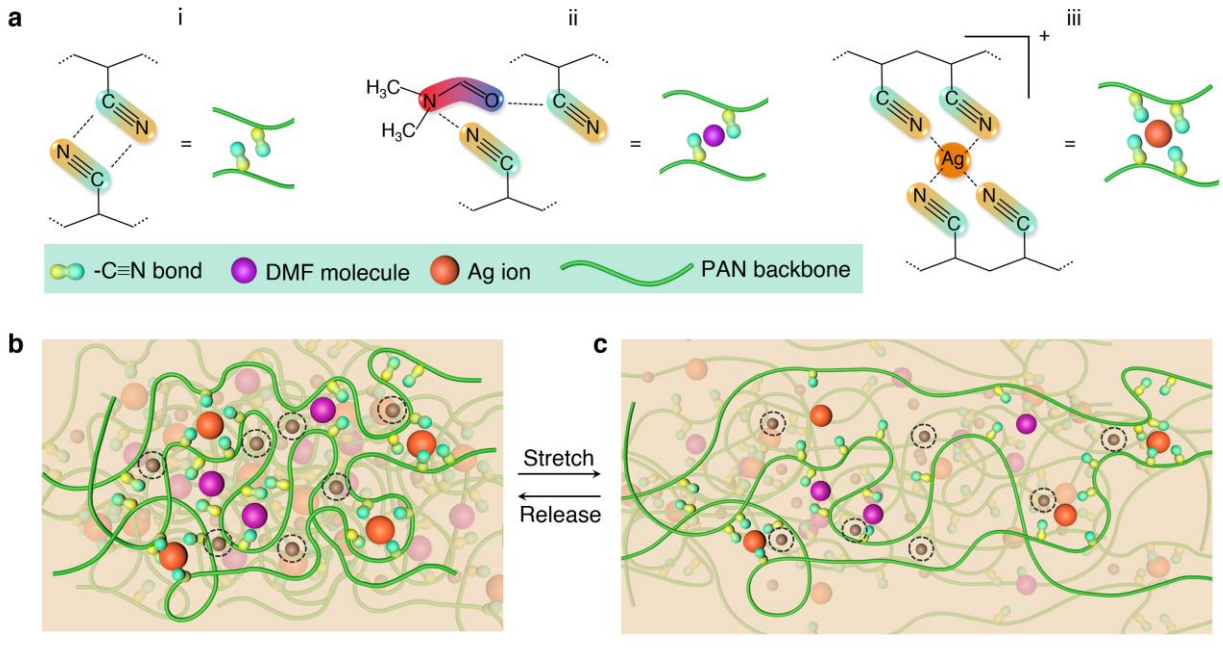

Supplementary Figure 20 | Schematic of PANSion chain network. a, Primary molecular interactions within PANSion film. **b**, Schematic showing the network evolution with $[Ag(-C\equiv N)_x]^+$ complexes dissociation-reformation during cyclic stretching.

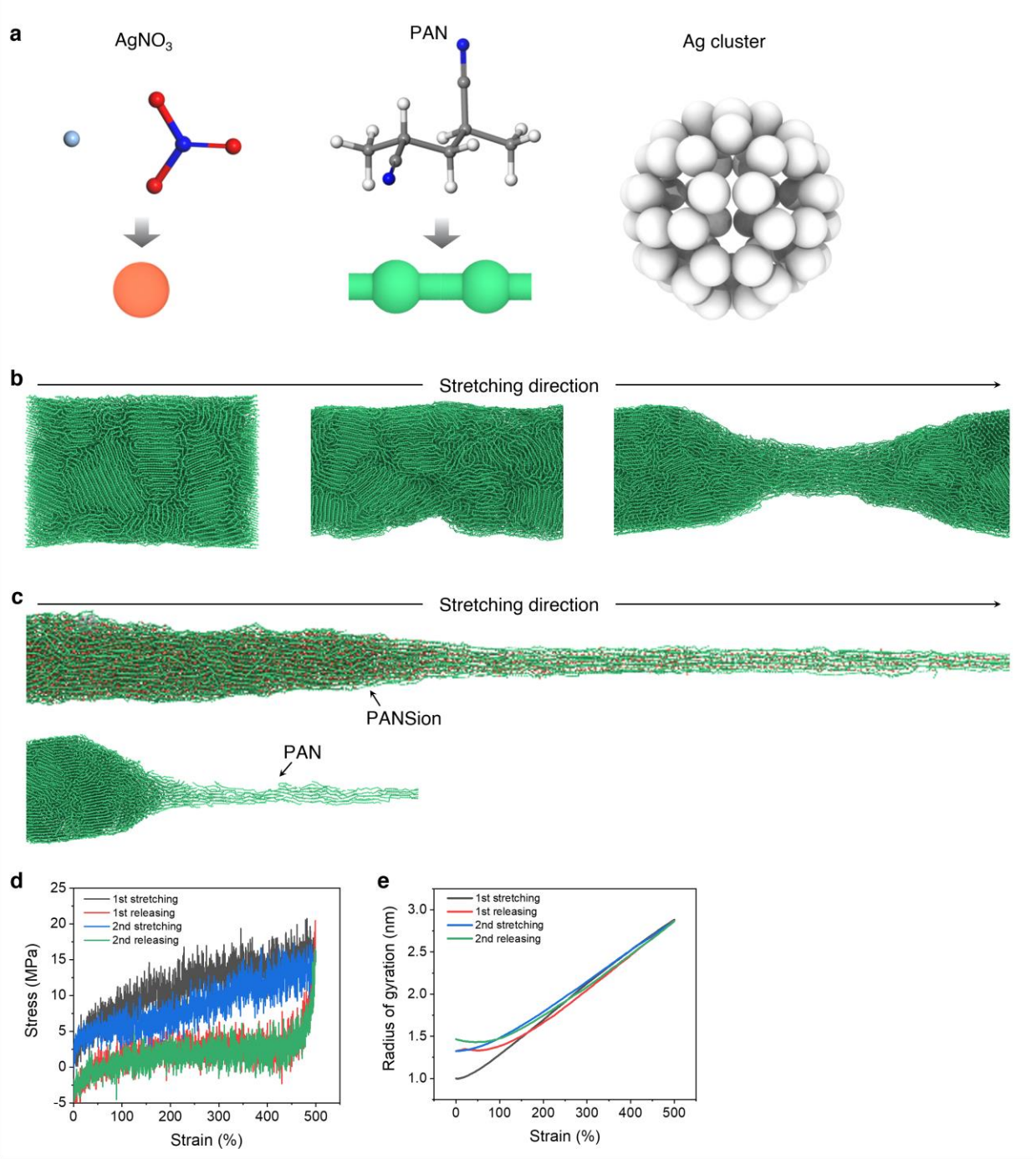

Supplementary Figure 21 | CG-MD results for PAN and PANSion films. a, The elements used in CG-MD simulations. **b**, Snapshots for the structural evolution of PAN under stretching. **c**, Snapshots for the failures of PAN and PANSion films. **d** and **e**, Stress-strain curves (d) and evolution of the radius of gyration (e) from two cycles of CG-MD results.

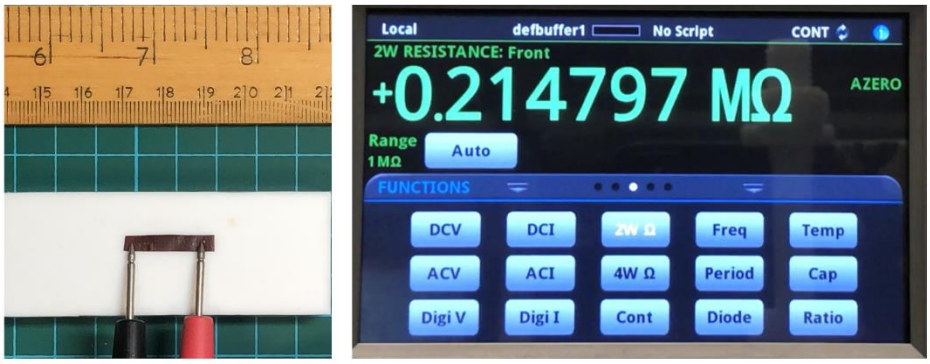

Supplementary Figure 22 | Two-wire resistance test for PANSion film. The resistance of PANSion film is in the range of MΩ.

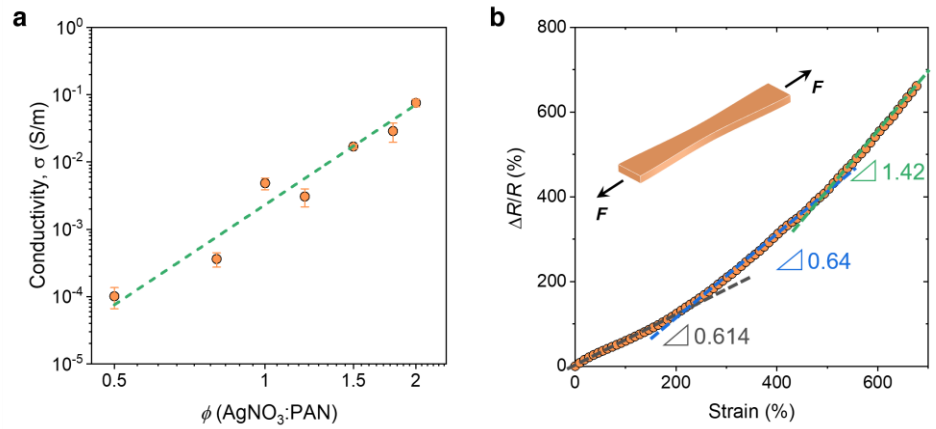

Supplementary Figure 23 | Electrical properties of PANSion film. a, Conductivity of PANSion film as a function of ϕ. **b**, The relationship between resistivity change ($\Delta R/R$ (%)) and strain (%). Inset is a schematic of PANSion film under stretching.

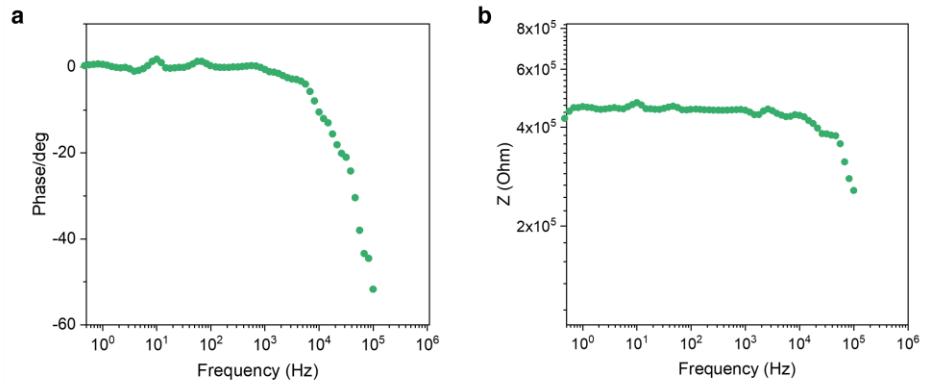

Supplementary Figure 24 | Impedance characterization of PANSion film.

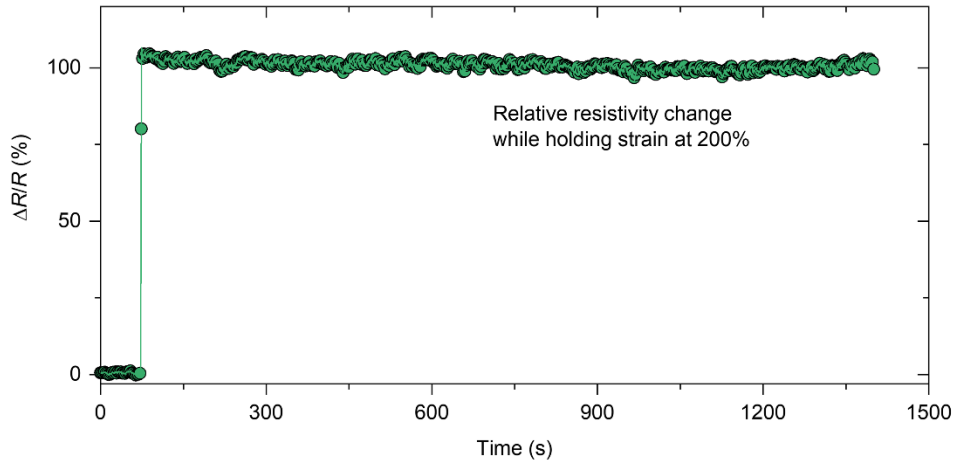

Supplementary Figure 25 | Stability of resistance change at a 200% strain. The resistivity change, $\Delta R/R$ (%), is relatively stable even at a continuous holding for ~30 min, indicating the network relaxation is limited.

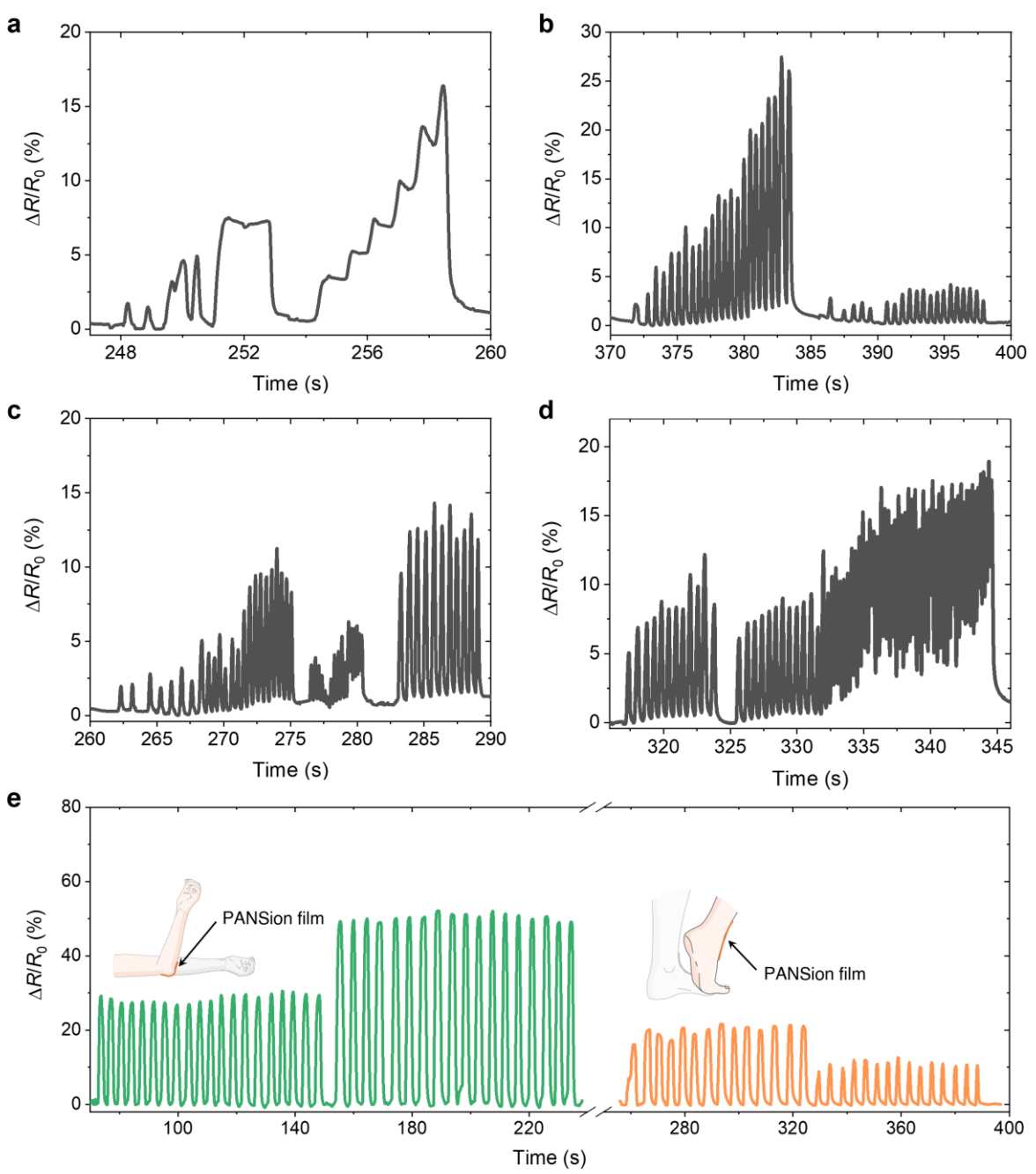

Supplementary Figure 26 | Sensing demonstrations of PANSion film body motion detections. **a**–**d**, Monitoring the agile movement of the index finger with various statuses, including different activity intensities and frequencies. **e**, Limb motions monitoring of elbow bending and ankle plantarflexion.

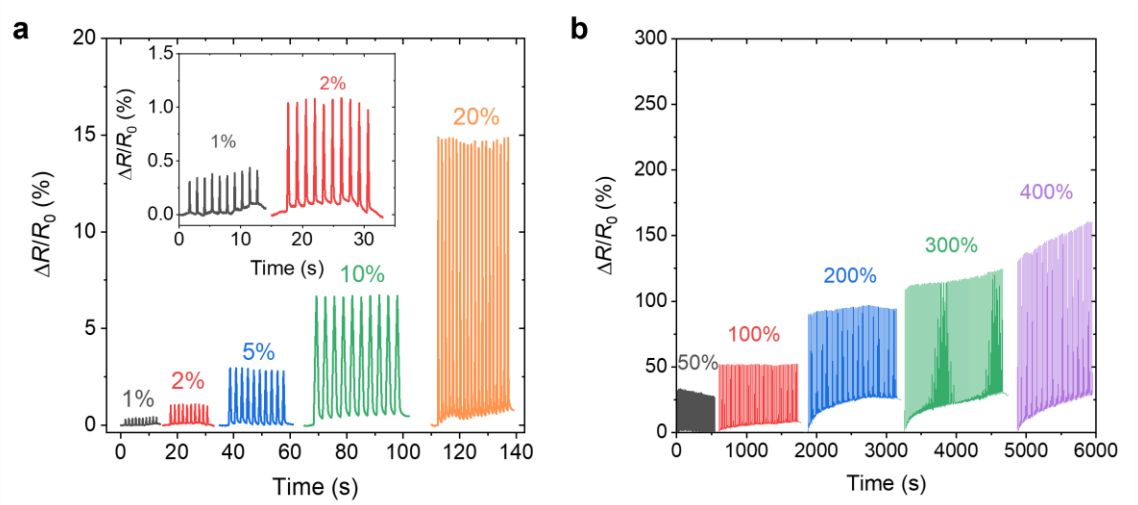

Supplementary Figure 27 | Sensing properties of PANSion film at various strains. a, Sensing data from cyclic tests at small strain from 1% to 20%. **b**, Sensing data from cyclic tests at large strain from 50% to 400%. PANSion film shows a fast strain recovery when the applied external extension is small so that the sensing performance within the small strain range is highly stable with a nearly unchanged baseline. When the applied strain is increased, a baseline shift-up is observed during the continuous cyclic test.

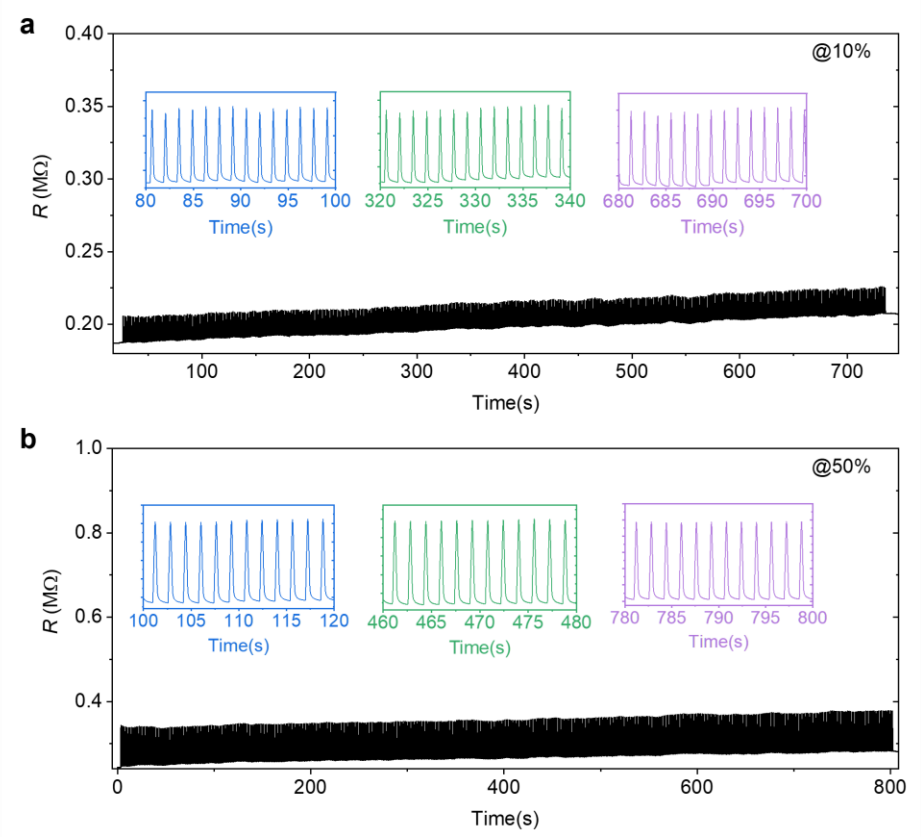

Supplementary Figure 28 | Stability of sensing performance. a and **b**, The cyclic sensing performance of PANSion film at a strain of 10% (a) and 50% (b) for 500 cycles. During the time range of testing, stable sensing output was observed for 10% and 50% strain (insets). While extending the testing time (namely, the testing cycles), the baseline is leveling up. However, the relative resistance change is stable for each tested strain.

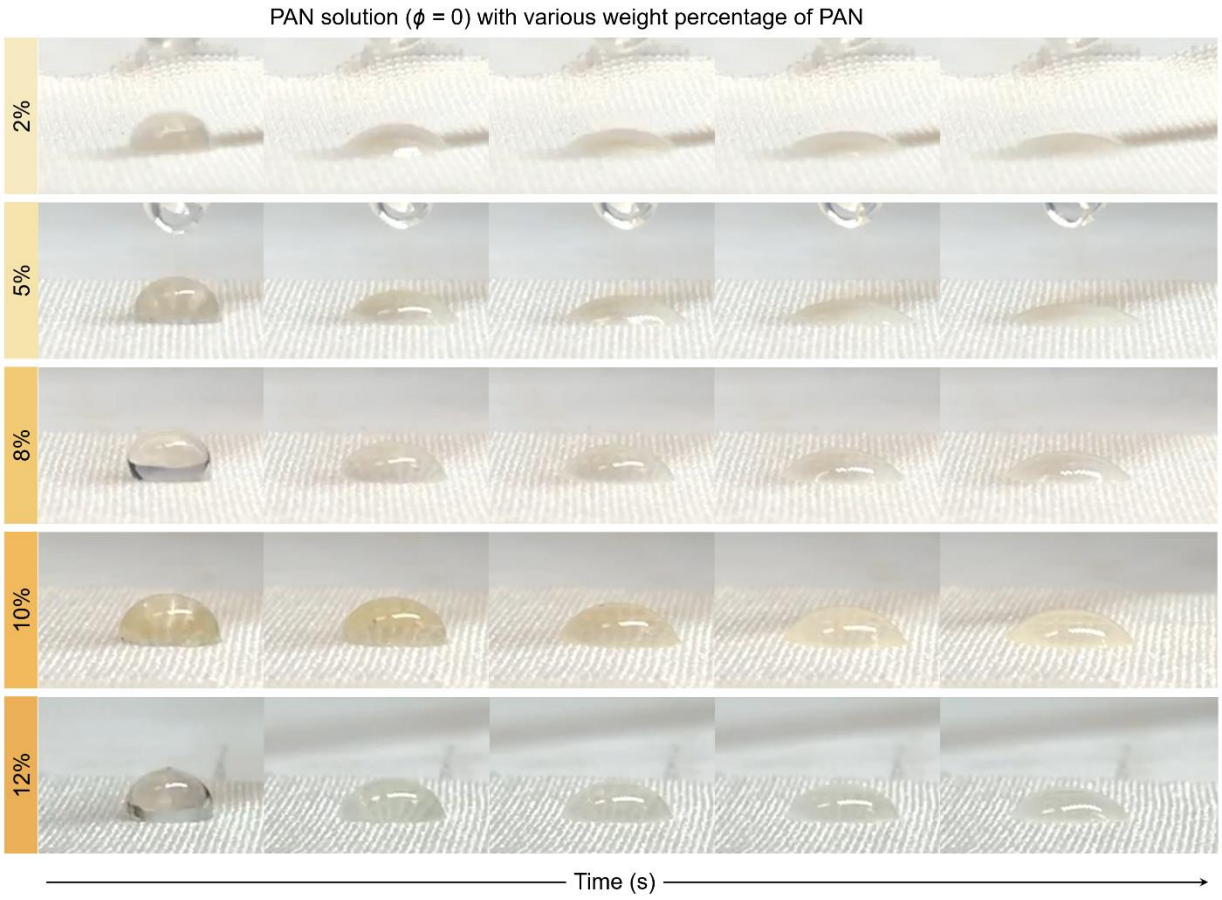

Supplementary Figure 29 | Penetration property of PAN solutions on a knitted PU fabric. As the concentration of PAN is increased (from 2 wt% to 12 wt%), the viscosity is also increased, leading to a slow penetration process into the PU fabric. Nevertheless, even for the 12 wt% PAN solution, good spreadability is observed.

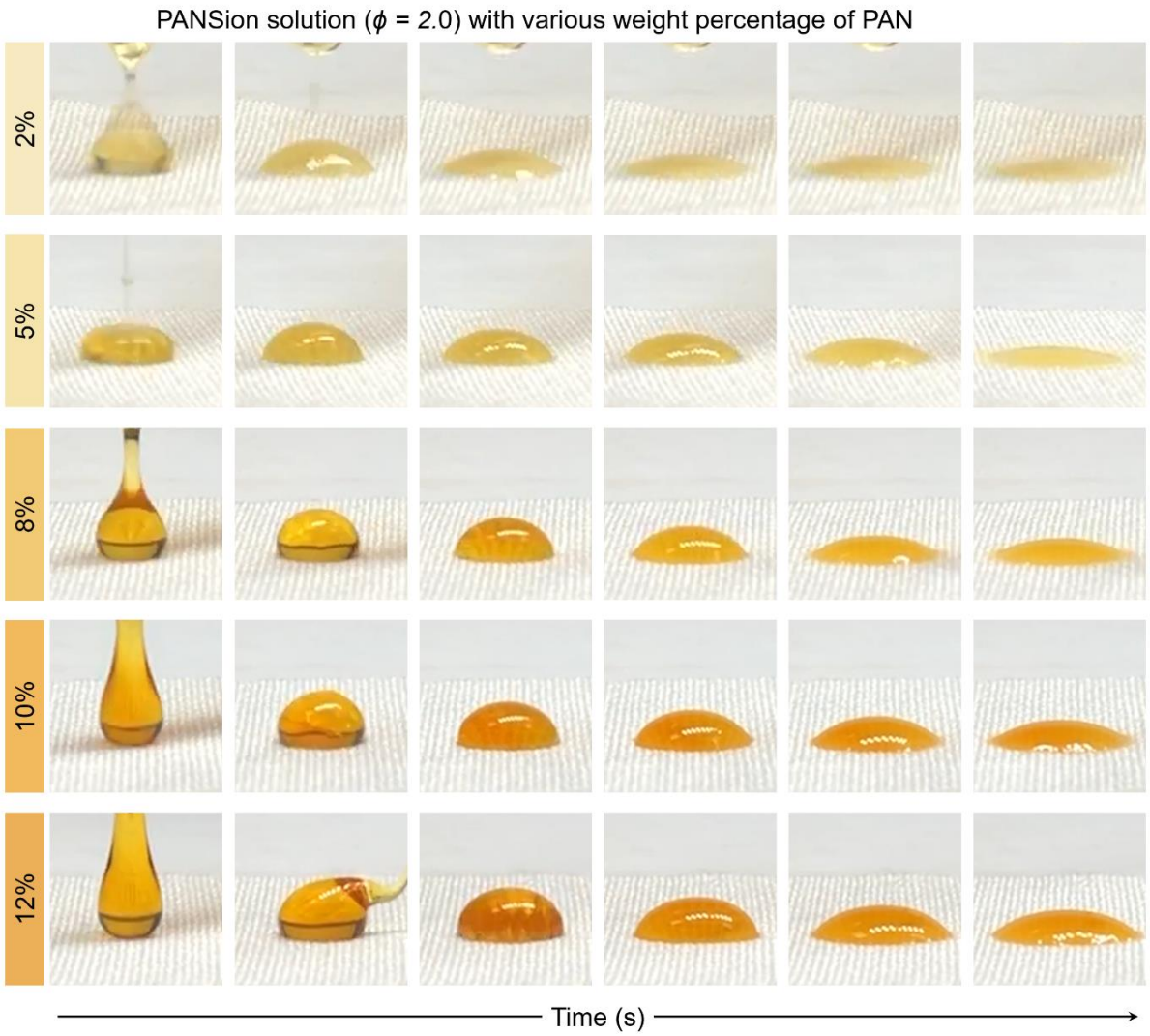

Supplementary Figure 30 | Penetration property of PANSion solutions on a knitted PU fabric. Although the addition of $AgNO_3$ increased the viscosity of PANSion solutions as compared to the corresponding PAN solution at the same PAN concentration, similar spreadability performance was observed. This is important, especially for the PANSion solution (ϕ = 2.0) with 10 wt% and 12 wt% of PAN. At this high concentration of PAN, the corresponding coated fabric could be guaranteed to form a continuous PANSion network, thus, enabling a sensing feature for the fabric.

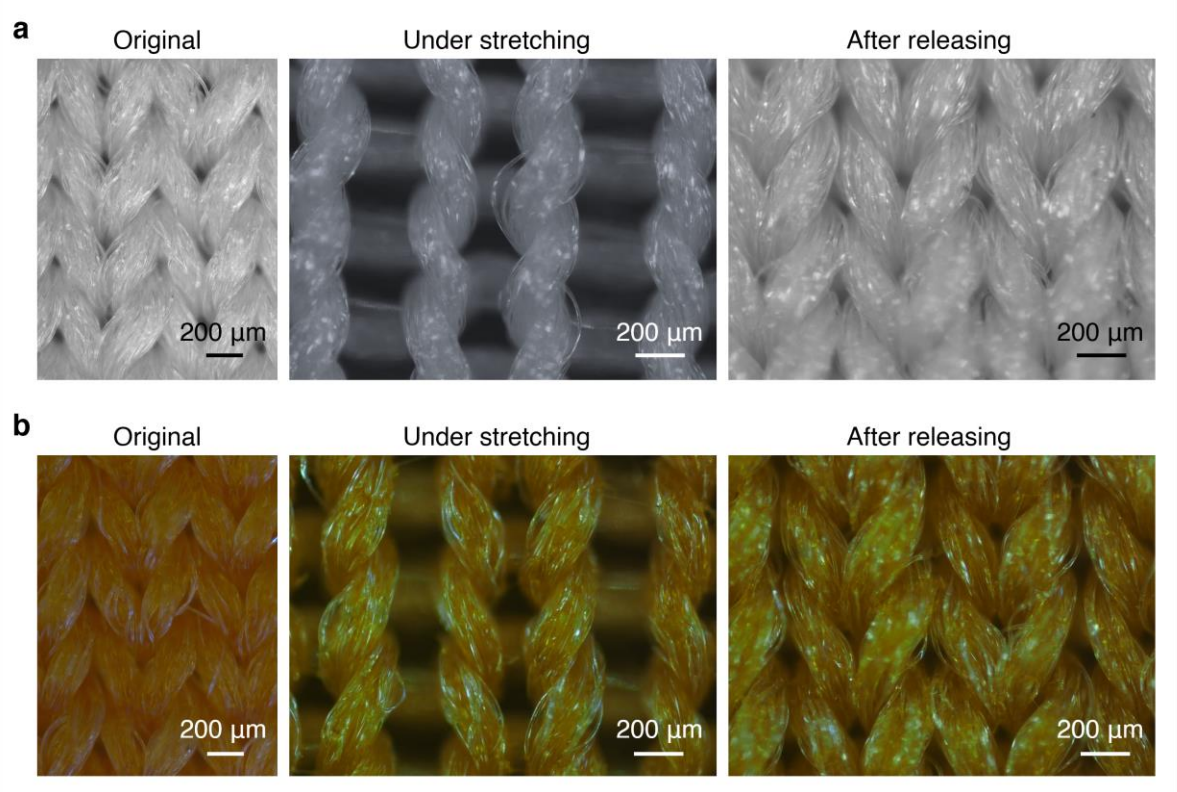

Supplementary Figure 31 | Stretchability and sensing performance of PANSion coated PU fabric. a and **b**, Optical images of PU fabric without (a) and with (b) PANSion coating, showing the microstructure morphology changes when subjected to mechanical stretch. Due to the good stretchability of the PANSion polymer, the coated PU fabric displays a similar stretching-releasing feature as compared to the uncoated one.

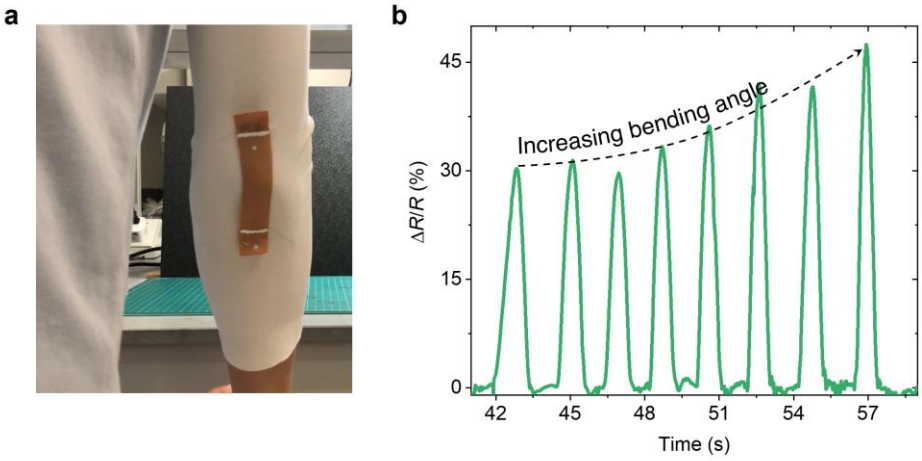

Supplementary Figure 32 | PANSion coated fabric for limb motion detection. a, A coated PU fabric is sewed into a sleeve. Since the mechanical property of a coated PU fabric is as similar as the uncoated one, it can be readily sewed into a sleeve as a smart patch for motion detection (e.g., elbow bending). **b**, The electrical response from the smart patch when the elbow is bending to different angles.

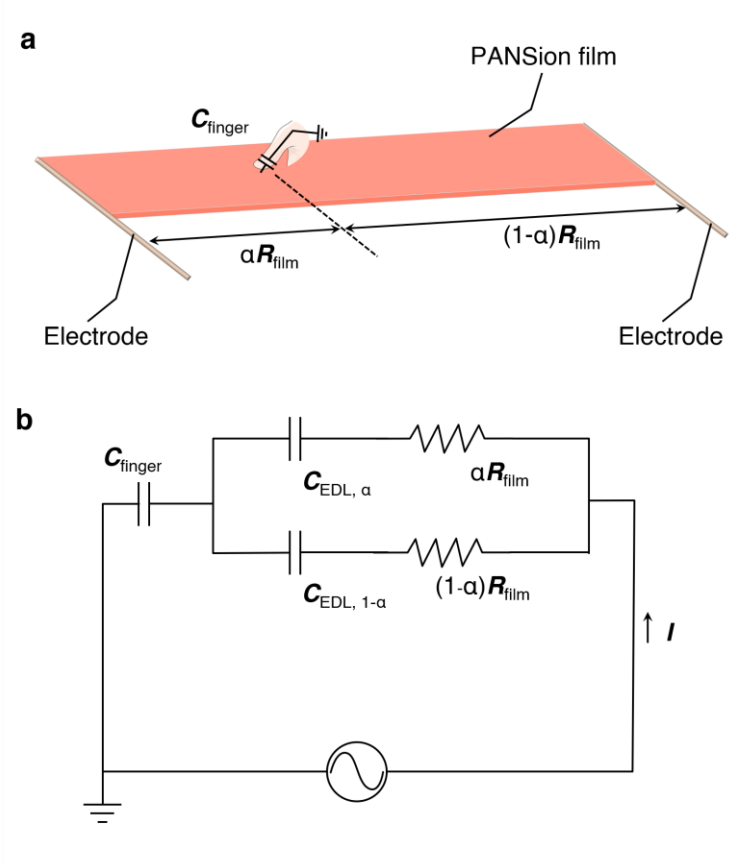

Supplementary Figure 33 | Surface capacitance mechanism. a, Schematic of a PANSion film during a point touch by a finger. **b**, The equivalent electric circuit diagram of the PANSion film upon finger touching.

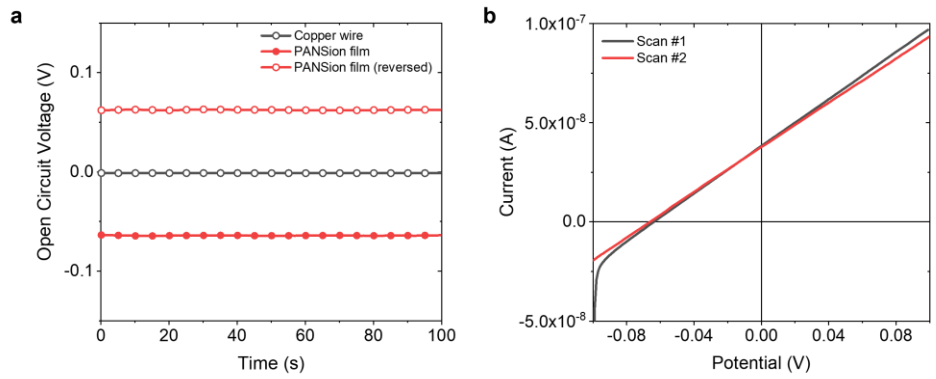

Supplementary Figure 34 | Open circuit voltage and potential-current scan curves of PANSion film. a, Open circuit voltage was recorded for PANSion film. For comparison, copper wire was scanned as a reference of electrical conductors. **b**, I-V curves of PANSion film, indicating an ohmic resistance feature. Interesting, there is a leakage current when the applied potential is zero, requiring us to conduct more investigation in future studies.

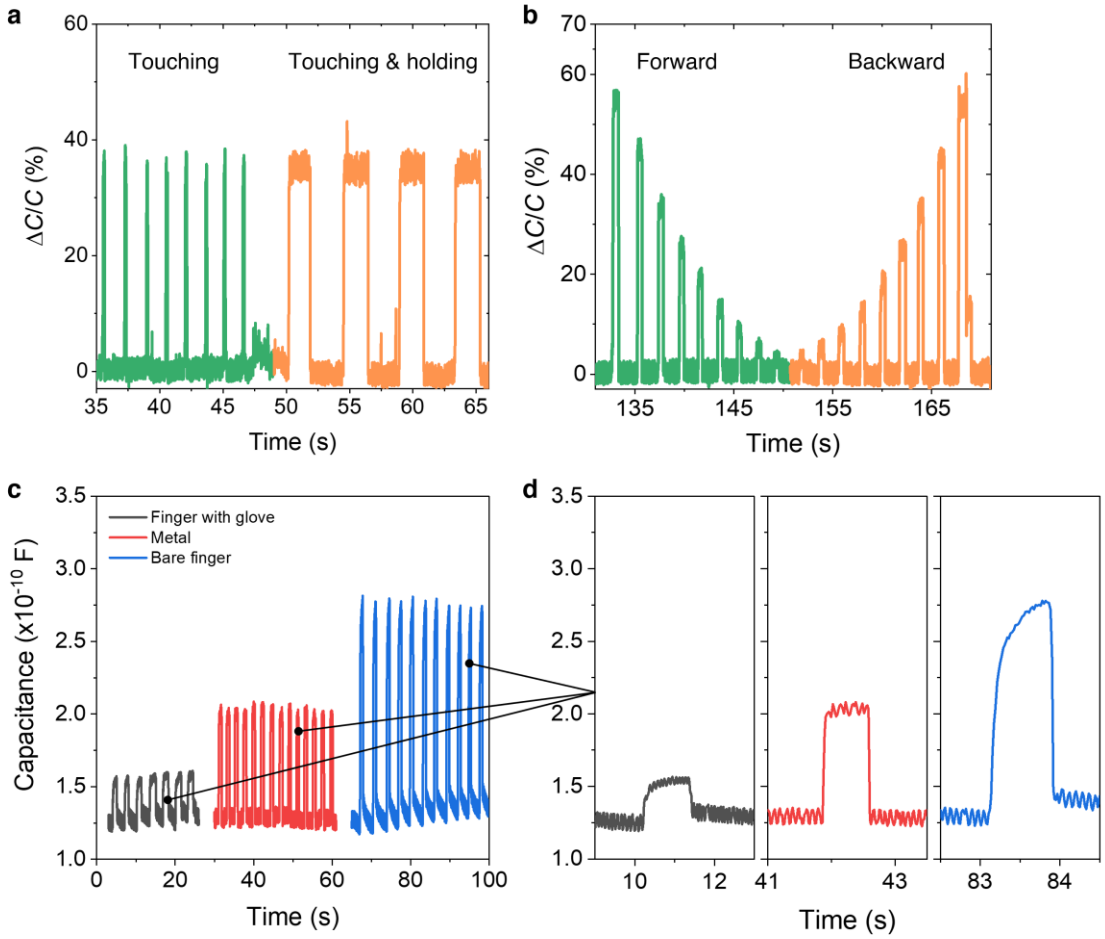

Supplementary Figure 35 | Sensing performance of PANSion film based on capacitance mechanism. a, Capacitance change to the stimulus of touch and touch-hold by a metal bar. **b**, Capacitance change when the touch point is moving along the PANSion film forward and backward. **c** and **d**, Capacitance change of PANSion film to different touch objects (c) and the corresponding different responding signal features (d).

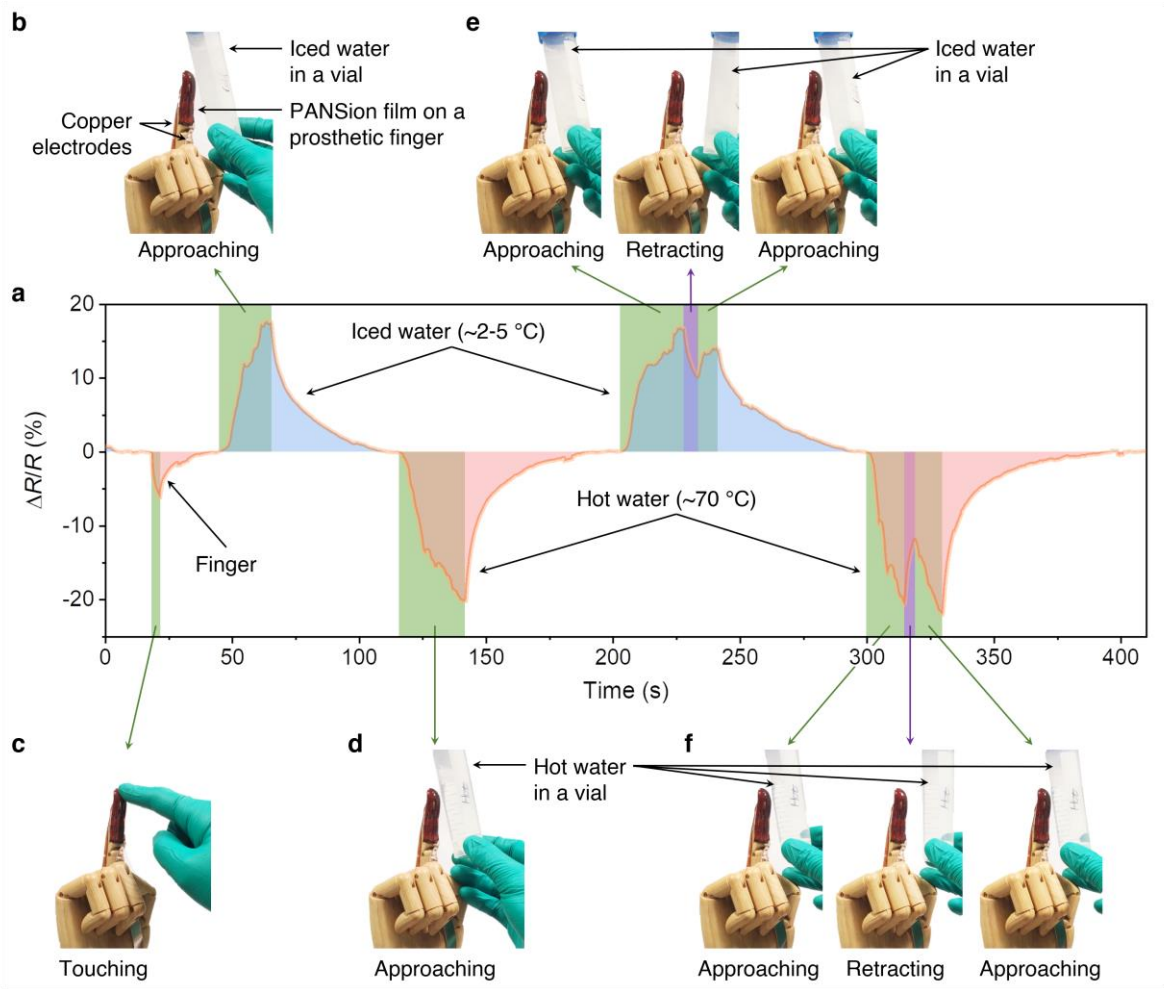

Supplementary Figure 36 | Sensing response of PANSion film to thermal disturbance. a, A resistance change curve displays sensing responses from a prosthetic finger with PANSion e-skin to environmental temperature variations, including finger touching (~37 ℃), and alternating cold (iced water, ~2-5 ℃)/warm (hot water, ~70 ℃) object approaching and retracting. Both iced and hot water could result in a resistance change of PANSion "skin". **b**, When a cold object is in close proximity to the prosthetic finger, a resistance increase is recorded. **c**–**d**, When a warm object is in close proximity to the prosthetic finger, a resistance decrease is recorded. **e**, The alternation between approaching and retracting a vial with iced water results in a concomitant increase and decrease of resistance. **f**, The alternation between approaching and retracting a vial with hot water results in a concomitant decrease and increase of resistance.

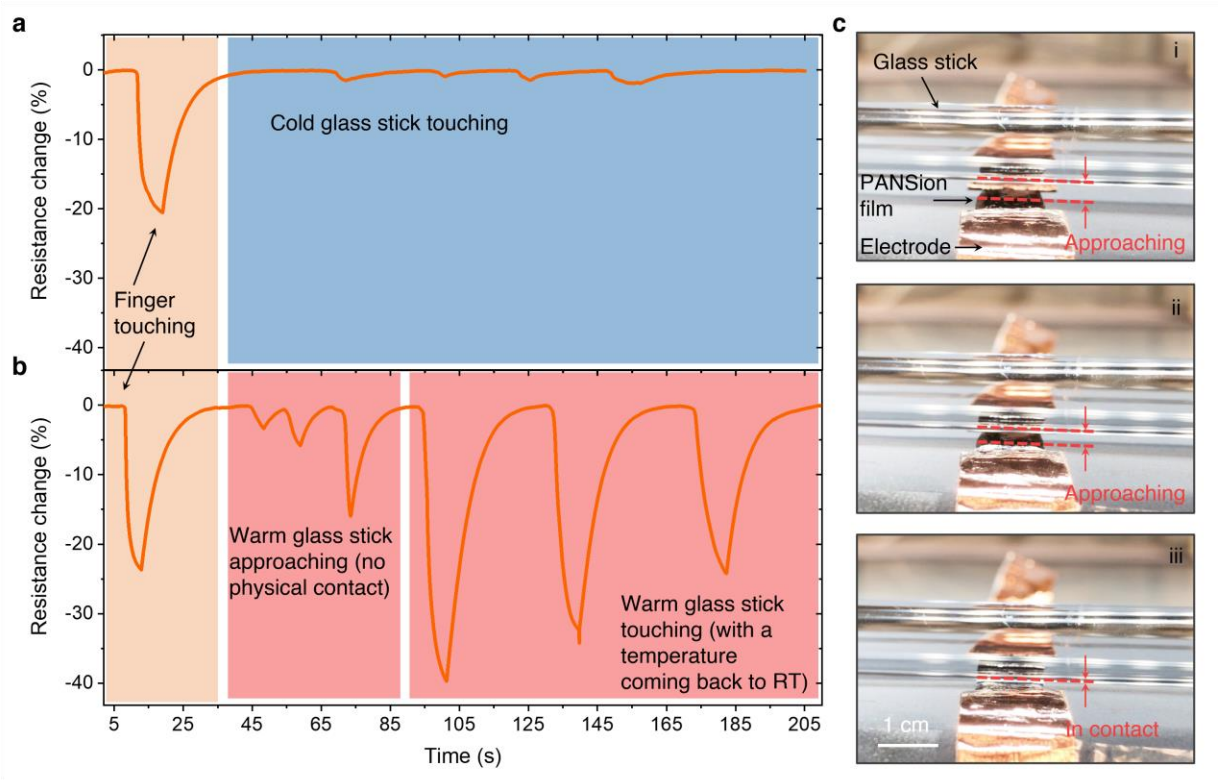

Supplementary Figure 37 | Sensing response of PANSion film to a cold and warm glass stick. **a**, The resistance change of PANSion film to finger touch followed by a room temperature glass stick touching. **b**, The resistance change of PANSion film to finger touch followed a warm glass stick approaching and touching (the temperature of the warm glass stick gradually comes back to room temperature). **c**, The touch procedure of a warm glass stick on the PANSion film.

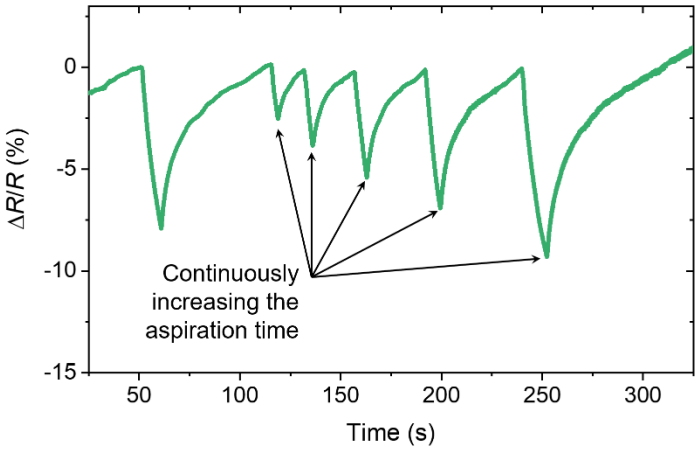

Supplementary Figure 38 | Sensing response of PANSion film to expirations. Since the temperature rise-upward or drop-downward is a gradual process for PANSion, it can be seen that a long expiration leads to a higher temperature rise (larger resistance change), and short expiration leads to a smaller temperature rise (lower resistance change).

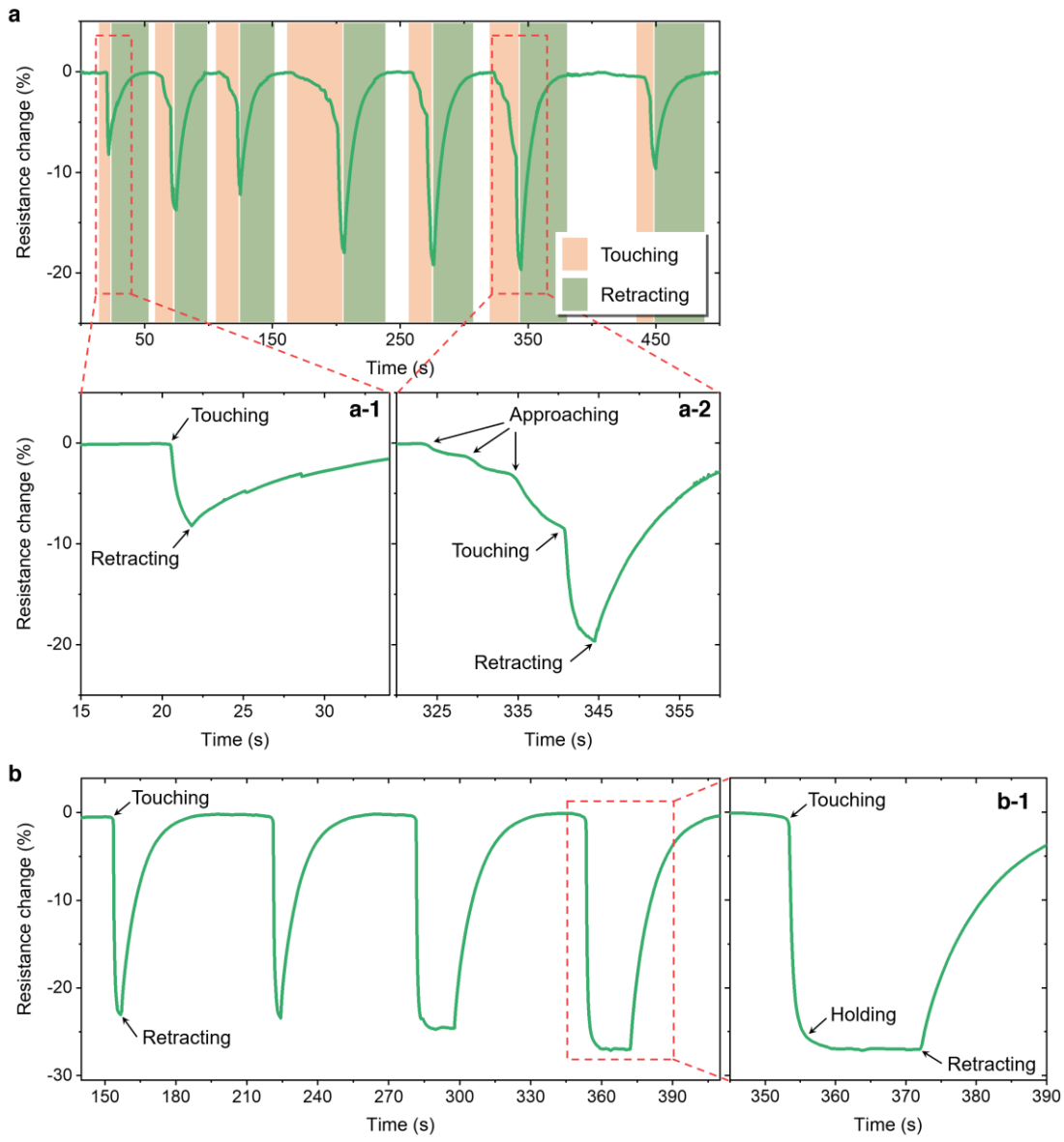

Supplementary Figure 39 | Sensing responses of PANSion film to finger approaching, touching and holding. a, Cyclic finger touches. A short period of touch results in a small resistance change, while a long period of touch results in a large resistance change. This is because the equilibrium temperature of the PANSion e-skin is leveling up gradually due to the slow heat-transfer nature occurring between the human finger and PANSion. (a-1) The touching and retracting points from the sensing response curve during a one touch cycle. (a-2) The approaching, touching, and retracting points from the sensing response curve of long-period touch. **b**, Sensing responses of a finger touching-retracting and touching-holding-retracting procedure. (b-1) Enlarged area of the touching-holding-retracting procedure from (B), clearly showing the starting point of each procedure of touching, holding, and retracting.

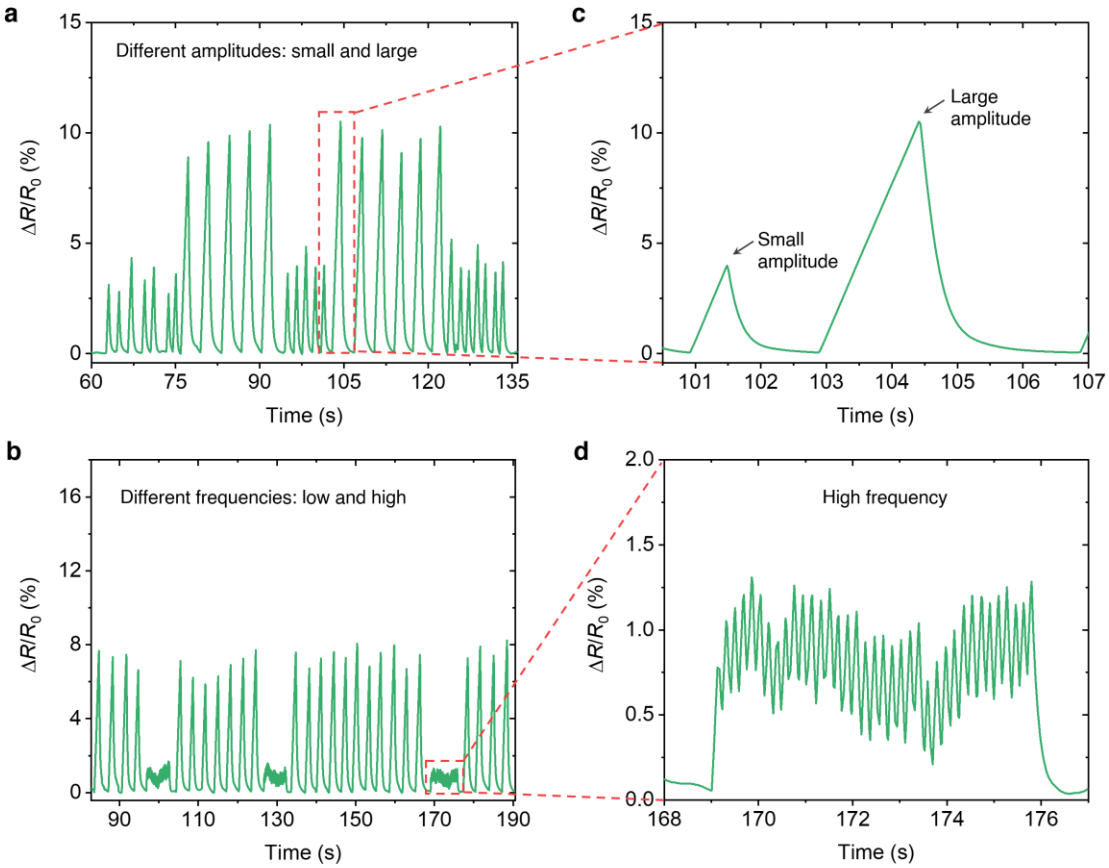

Supplementary Figure 40 | Self-sensing actuation performance of PANSion film. a and **b**, Sensing responses for actuations with both small/large amplitudes (a) and low/high frequencies (b) under zero load. **c** and **d**, Enlarged area of two actuation cycles that correspond to small and large amplitudes (c) and continuous actuation at high frequency (d).

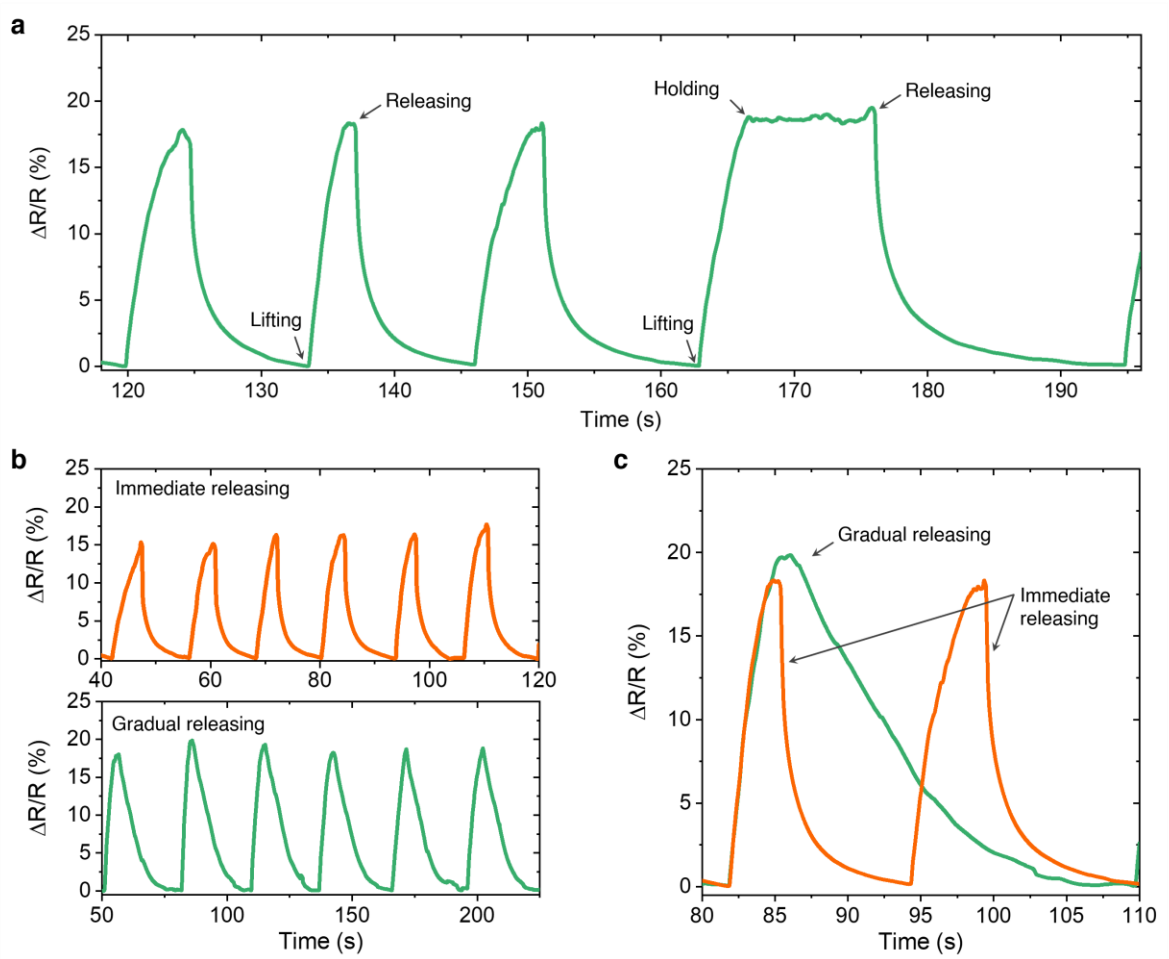

Supplementary Figure 41 | Sensing responses of PANSion film actuator when performing weigh-lifting task. a, Sensing responses for weight-lifting, including lifting-releasing and lifting-holding-releasing procedures. The starting point of lifting and releasing can be easily recognized from the resistance change pattern. **b**, Cyclic sensing responses of weight-lifting with two releasing procedures, including immediate releasing (top) and gradual releasing (bottom). **c**, Comparison of electrical signals between the immediate and gradual releasing procedure.

Supplementary Table 1 | Comparisons of PANSion to biological muscle and other engineering actuators with regards to unification of sensing and actuation in a single material system.

Sensing				Actuation					Refs
Stretch-ability %	Multi modal sensing	Self-healing	Processing difficulty	Self-sensing	Specific work J/kg	Specific power W/kg	Weight-lifting capability	Working principle	
1200	✓[a]	n/a[b]	Low	✓ (built-in)[c]	350	500	3700×[d]	Pneumatic	This work
300	✗[e]	✓	High	✗	215	488	3000×		[11]
124	✗	n/a	Medium	✓ (add-on)[f]	70	614	4-kg	hydraulic	[12]
1000	✗	n/a	Medium	✗	n/a	75	650×		[13]
n/a	✗	n/a	n/a	✗	3.7	18.5	n/a		[14]
200	✗	✓	Easy	✗	179	n/a	193×		[15]
n/a	✗	n/a	Medium	✗	n/a	160	n/a	hydraulic	[16]
~300	✓	✓	Hard	✗	n/a	n/a	3.4×[g]	Pneumatic	[17]
~70	✗	n/a	Hard	✓	n/a	n/a	20×	Thermal expansion	[18]
n/a	✓	n/a	Hard	✓ (add-on)	n/a	n/a	n/a	Pneumatic	[19]
2000	✗	✓	Easy	✗	n/a	n/a	n/a	-	[20]
n/a	✓	n/a	Easy	✓ (add-on)	n/a	n/a	n/a	Thermal expansion	[21]
~2500	✗	✓	Easy	✗	n/a	n/a	n/a	Dielectric actuator	[3]
~10	✗	n/a	Medium	✗	1360	27900	41-MPa	Thermal expansion	[22]
~4.5	✗	n/a	Medium	✗	2630	5260	140-MPa	Thermal expansion	[23]
~50	✗	n/a	Medium	✗	n/a	n/a	n/a	Hydraulic	[24]
n/a	✗	n/a	Easy	✓ (add-on)	n/a	n/a	n/a	Pneumatic	[25]
n/a	✗	n/a	Easy	✓ (built-in)	n/a	n/a	n/a	Hydraulic	[26]
~480	✓	n/a	Medium	✓ (add-on)	n/a	n/a	n/a	Pneumatic	[27]
n/a	✓	n/a	Easy	✓ (add-on)	n/a	n/a	n/a	-	[28]
n/a	✓	n/a	Medium	✓ (add-on)	n/a	n/a	n/a	Pneumatic	[29]
-	✓	✓	-	✓ (built-in)	-	50-300	-	Biological muscle	[14]

[a] Indicating yes for the specific property
[b] Indicating the property is not mentioned in the reference
[c] The self-sensing property is seamlessly integrated with actuators as a built-in function.
[d] Indicating the number of how many times compared to the weight of actuator itself
[e] Indicating no for the specific property.
[f] The self-sensing property is introduced to actuators by integrating additional sensing parts as an add-on function.
[g] Value calculated using data in the reference.

Supplementary Table 2 | Binding energies of possible metal-ligand complexes using PAN molecule as ligand.

B	PAN
E_B (Hatree)	–382.2132768

A	Ca^{2+} ($CaCl_2$)	Mg^{2+} ($MgSO_4$)	Zn^{2+} ($ZnCl_2$)	Fe^{2+} ($FeCl_2$)	Cu^{2+} ($CuSO_4$)	Cu^{+} (CuCl)	Au^{+} (AuCl)	Ag^{+} ($AgNO_3$)
E_A (Hatree)	–1598.2072917	–899.2518473	–2700.1455000	–1962.9955769	–2339.8517159	–2100.9834710	–18331.0656698	–5480.7873544
E_{AB} (Hatree)	–1980.5066521	–1281.5470526	–3082.4291060	–2345.2988139	–2722.1463179	–2483.2777416	–18713.3269795	–5863.0518773
$E_{binding}$ (Hatree)	–0.0860836	–0.0819285	–0.0703292	–0.0899602	–0.0813252	–0.0809938	–0.0480329	–0.0512461
$E_{binding}$ (kJ/mol)	–226.0124918	–215.10327675	–184.6493146	–236.1905051	–213.5193126	–212.6492219	–126.11037895	–134.54663555

Supplementary Table 3 | Compositions of PANSion solutions with varying weight ratios (ϕ) between $AgNO_3$ and PAN and the corresponding mole ratio between Ag^+ and –C≡N.

	$AgNO_3$ (mg)	PAN (mg)	$AgNO_3$:PAN (ϕ)	–C≡N* (mole)	Ag^+ (mole)	–C≡N:Ag^+ (λ)
Control	0	200	0	0.003774	0	0.0
Group #1	100	200	0.5	0.003774	0.0005887	6.4102
Group #2	200	200	1.0	0.003774	0.001177	3.2051
Group #3	300	200	1.5	0.003774	0.001766	2.1367
Group #4	400	200	2.0	0.003774	0.002354	1.6025

Note: the mole of –C≡N is estimated based on the average molecule weight of PAN at 150,000 with a repeat unit of $[C_3H_3N]_n$.

Supplementary Table 4 | Percentage of remaining DMF in PAN and PANSion films.

ϕ	0.0	0.5	1.0	1.5	2.0
DMF (wt%)	8.04	21.63	27.04	30.08	30.67

Supplementary Table 5 | Parameters of non-bonded interactions.

$\epsilon_{ij}/\sigma_{ij}$	*A*	*B*	*C*
A	$0.0895\epsilon_0/0.89\sigma_0$	$0.895\epsilon_0/0.687\sigma_0$	$0.448\epsilon_0/0.80\sigma_0$
B		$0.0895\epsilon_0/0.89\sigma_0$	$0.448\epsilon_0/0.80\sigma_0$
C			$0.0895\epsilon_0/0.89\sigma_0$

Supplementary Video 1 | CG-MD simulation. The cyclic stretching-releasing of PANSion film and stretching-to-break of PAN film.

Supplementary Video 2 | PANSion film as eskin for object touch (haptic) sensing and aspiration detection.

Supplementary Video 3 | Pneumatic PANSion actuator with the self-sensing ability of deformation amplitude and frequency.

Supplementary Video 4 | PANSion actuator cyclically lifts a 50-g load with the self-sensing ability of the whole lifting-releasing process.

Supplementary Video 5 | PANSion actuator lifts a 100-g load with different actuation patterns including lifting-holding, and lifting-controlled-releasing. These patterns are readily recognizable from the corresponding real-time electrical signals.

Supplementary Video 6 | Demonstration of the manipulating object (at different temperatures) using a soft gripper based on a PANSion actuator with a two-chamber configuration. at different temperatures using a PANSion-based gripper.

Supplementary References

1. Zhu, Y.-L., et al., *GALAMOST: GPU-accelerated large-scale molecular simulation toolkit.* Journal of Computational Chemistry, 2013. **34**(25): p. 2197-2211.
2. Deng, Y., et al., *Enzymatic biosynthesis and immobilization of polyprotein verified at the single-molecule level.* Nat. Commun., 2019. **10**(1): p. 2775.
3. Li, C.H., et al., *A highly stretchable autonomous self-healing elastomer.* Nat. Chem., 2016. **8**(6): p. 618–624.
4. Eom, Y. and B.C. Kim, *Solubility parameter-based analysis of polyacrylonitrile solutions in N,N-dimethyl formamide and dimethyl sulfoxide.* Polymer, 2014. **55**(10): p. 2570-2577.
5. Zhang, S., et al., *A Highly Stretchable Polyacrylonitrile Elastomer with Nanoreservoirs of Lubricant Using Cyano-Silver Complexes.* Nano Lett., 2019. **19**(6): p. 3871–3877.
6. Pastoriza-Santos, I. and L.M. Liz-Marzán, *N,N-Dimethylformamide as a Reaction Medium for Metal Nanoparticle Synthesis.* Adv. Funct. Mater., 2009. **19**(5): p. 679–688.
7. Pastoriza-Santos, I. and L.M. Liz-Marzán, *Synthesis of Silver Nanoprisms in DMF.* Nano Lett., 2002. **2**(8): p. 903-905.
8. Pastoriza-Santos, I. and L.M. Liz-Marzán, *Formation and Stabilization of Silver Nanoparticles through Reduction by N,N-Dimethylformamide.* Langmuir, 1999. **15**(4): p. 948–951.
9. Barwich, S., et al., *On the relationship between morphology and conductivity in nanosheet networks.* Carbon, 2020.
10. Cunningham, G., et al., *Percolation scaling in composites of exfoliated MoS2 filled with nanotubes and graphene.* Nanoscale, 2012. **4**(20): p. 6260-4.
11. Pena-Francesch, A., et al., *Biosynthetic self-healing materials for soft machines.* Nat. Mater., 2020. **19**(11): p. 1230–1235.
12. Acome, E., et al., *Hydraulically amplified self-healing electrostatic actuators with muscle-like performance.* Science, 2018. **359**(6371): p. 61–65.
13. Kanik, M., et al., *Strain-programmable fiber-based artificial muscle.* Science, 2019. **365**(6449): p. 145–150.
14. Yang, D., et al., *Buckling Pneumatic Linear Actuators Inspired by Muscle.* Adv. Mater. Technol., 2016. **1**(3): p. 1600055.
15. Ford, M.J., et al., *A multifunctional shape-morphing elastomer with liquid metal inclusions.* Proc. Natl. Acad. Sci., 2019. **116**(43): p. 21438–21444.
16. Kellaris, N., et al., *Peano-HASEL actuators: Muscle-mimetic, electrohydraulic transducers that linearly contract on activation.* Sci. Robot., 2018. **3**(14): p. eaar3276.
17. Baumgartner, M., et al., *Resilient yet entirely degradable gelatin-based biogels for soft robots and electronics.* Nat. Mater., 2020. **19**: p. 1102–1109
18. Zhao, Y., et al., *Somatosensory actuator based on stretchable conductive photothermally responsive hydrogel.* Sci. Robot., 2021. **6**(53): p. eabd5483.
19. Truby, R.L., et al., *Soft Somatosensitive Actuators via Embedded 3D Printing.* Adv. Mater., 2018. **30**(15): p. 1706383.
20. Cao, Y., et al., *Self-healing electronic skins for aquatic environments.* Nat. Electron., 2019. **2**(2): p. 75–82.
21. Chen, L., et al., *Graphene-Based Actuator with Integrated-Sensing Function.* Adv. Funct. Mater., 2019. **29**(5).

22. Lima, M.D., et al., *Electrically, Chemically, and Photonically Powered Torsional and Tensile Actuation of Hybrid Carbon Nanotube Yarn Muscles.* Science, 2012. **338**(6109): p. 928.
23. Haines, C.S., et al., *Artificial Muscles from Fishing Line and Sewing Thread.* Science, 2014. **343**(6173): p. 868.
24. Cacucciolo, V., et al., *Stretchable pumps for soft machines.* Nature, 2019. **572**(7770): p. 516-519.
25. Kure, K., et al., *Flexible displacement sensor using injected conductive paste.* Sens. Actuator A Phys., 2008. **143**(2): p. 272-278.
26. Helps, T. and J. Rossiter, *Proprioceptive Flexible Fluidic Actuators Using Conductive Working Fluids.* Soft Robot., 2017. **5**(2): p. 175-189.
27. Larson, C., et al., *Highly stretchable electroluminescent skin for optical signaling and tactile sensing.* Science, 2016. **351**(6277): p. 1071.
28. Rocha, R.P., et al., *Fabrication and characterization of bending and pressure sensors for a soft prosthetic hand.* Journal of Micromechanics and Microengineering, 2018. **28**(3): p. 034001.
29. Yang, H., et al., *A novel pneumatic soft sensor for measuring contact force and curvature of a soft gripper.* Sens. Actuator A Phys., 2017. **266**: p. 318-327.